

## Transmission stabilization in soliton-based optical-waveguide systems by frequency-dependent linear gain-loss and the Raman self-frequency shift

Avner Peleg<sup>1,\*</sup> and Debananda Chakraborty<sup>2</sup>

<sup>1</sup>*Department of Basic Sciences, Afeka College of Engineering, Tel Aviv 69988, Israel*

<sup>2</sup>*Department of Mathematics, New Jersey City University, Jersey City, New Jersey 07305, USA*



(Received 17 May 2018; published 30 July 2018)

We study transmission stabilization against radiation emission and enhancement of transmission quality in soliton-based nonlinear optical waveguides with weak linear gain-loss, cubic loss, and delayed Raman response. We show by numerical simulations with perturbed nonlinear Schrödinger propagation models that transmission quality in waveguides with frequency-independent linear gain and cubic loss is not improved by the presence of delayed Raman response due to the lack of an efficient mechanism for suppression of radiation emission. In contrast, we find that the presence of delayed Raman response leads to significant enhancement of transmission quality in waveguides with frequency-dependent linear gain-loss and cubic loss. Enhancement of transmission quality in the latter waveguides is enabled by the separation of the soliton's spectrum from the radiation's spectrum due to the Raman-induced self-frequency shift and by efficient suppression of radiation emission due to the frequency-dependent linear gain-loss. Further numerical simulations demonstrate that the enhancement of transmission quality in waveguides with frequency-dependent linear gain-loss, cubic loss, and delayed Raman response is similar to transmission quality enhancement in waveguides with linear gain, cubic loss, and guiding filters with a varying central frequency. Thus, our study demonstrates a general mechanism for stabilizing soliton transmission, which is based on the interplay between frequency-dependent linear gain-loss and perturbation-induced shifting of the soliton frequency.

DOI: [10.1103/PhysRevA.98.013853](https://doi.org/10.1103/PhysRevA.98.013853)

### I. INTRODUCTION

Transmission of solitons in nonlinear optical-waveguide systems has been the subject of intensive research in the last several decades due to the stability and shape-preserving properties of the solitons [1–4]. In addition, since Kerr nonlinearity does not cause any pulse distortion in single-soliton propagation, soliton-based transmission can be used to realize higher transmission rates and larger error-free transmission distances compared with other transmission methods [2,4–7]. This is true, for example, for transmission in optical fibers. Indeed, in Ref. [8], error-free optical fiber transmission of a single sequence of optical solitons at a bit rate of 10 Gb/s over  $10^6$  km was experimentally demonstrated by using synchronous modulation. In another experiment, error-free transmission of seven soliton sequences at 10 Gb/s per sequence over transoceanic distances was realized, using dispersion-tapered optical fibers and guiding filters with a varying central frequency [9]. Even larger transmission rates were experimentally demonstrated with dispersion-managed solitons. In particular, in Ref. [7], transmission of 25 sequences of dispersion-managed solitons at 40 Gb/s per sequence over 1500 km was achieved. Furthermore, transmission of 109 dispersion-managed soliton sequences at 10 Gb/s per sequence over  $2 \times 10^4$  km was demonstrated in Ref. [10].

In this paper, we study transmission stabilization of conventional optical solitons, that is, of solitons of the cubic nonlinear

Schrödinger (NLS) equation without dispersion management. Our reasons for considering conventional optical solitons are the following. First, as stated in the first paragraph, because of the stability and shape-preserving properties of the solitons, soliton-based transmission is advantageous compared with other transmission methods. Second, due to the integrability of the unperturbed cubic NLS equation, derivation of the equations for dynamics of the soliton parameters in the presence of perturbations can be done in a rigorous manner. Third, the simpler properties of conventional solitons compared with dispersion-managed solitons make them more suitable for usage in optical networks and in other optical systems, where simplicity and scalability are important. Fourth, even though the details of pulse dynamics in other transmission systems might be different, analysis of transmission stabilization of conventional optical solitons can still provide a rough idea on how to realize transmission stabilization in other waveguide setups.

In several earlier works, we developed a general method for stabilizing the dynamics of optical soliton amplitudes in multisequence nonlinear optical waveguide systems with weak nonlinear dissipation [11–18]. The method is based on showing that amplitude dynamics induced by the dissipation in  $N$ -sequence optical waveguide systems can be approximately described by  $N$ -dimensional Lotka-Volterra (LV) models. Stability analysis of the equilibrium states of the LV models can then be used for realizing stable amplitude dynamics along ultralong distances. However, due to the instability of multisequence soliton-based transmission against resonant and nonresonant emission of radiation, the distances along which stable amplitude dynamics was observed in numerical

\*Corresponding author: [avpeleg@gmail.com](mailto:avpeleg@gmail.com)

simulations with the perturbed NLS equation were initially limited to a few hundred dispersion lengths [12,13]. Further analysis showed that a major mechanism for transmission destabilization in these systems is associated with resonant emission of radiation during intersequence soliton collisions, where the emitted radiation undergoes unstable growth and develops into radiative sidebands [16,17,19]. Significant increase in the stable propagation distances was achieved by the introduction of frequency-dependent linear gain-loss in  $N$ -waveguide couplers [16–19]. It was shown in these works that the presence of frequency-dependent linear gain-loss leads to efficient suppression of the instability due to resonant radiation emission. The limiting cause for transmission instability in  $N$ -waveguide couplers with frequency-dependent linear gain-loss was associated with nonresonant radiation emission due to the effects of the dissipation on single-soliton propagation [16,18]. Therefore, the latter process is a serious obstacle for further enhancement of transmission stability in nonlinear optical waveguide systems, where conventional optical solitons are used.

In two of the recent works, where stable long-distance multisequence transmission with conventional solitons was demonstrated, the effects of delayed Raman response were taken into account in addition to the effects of frequency-dependent linear gain-loss [16,17]. The stable transmission distances achieved in these studies were larger by two orders of magnitude compared with the distances obtained in earlier studies, where the effects of frequency-dependent linear gain-loss and delayed Raman response were not taken into account [12,13]. It is known that the most important effect of delayed Raman response on single-soliton propagation in nonlinear optical waveguides is a continuous downshift of the soliton's frequency, which is called the Raman self-frequency shift [20–22]. In view of the findings in Refs. [16,17], it is important to investigate whether the combination of frequency-dependent linear gain-loss and one of the effects associated with delayed Raman response, such as the Raman self-frequency shift, can indeed lead to significant enhancement of transmission stability in soliton-based optical waveguide systems. If such transmission stabilization is possible, it is important to characterize the mechanism leading to the stabilization.

In this paper, we take on these important tasks by studying propagation of a single soliton in nonlinear optical waveguides with weak linear gain-loss, cubic loss, and delayed Raman response. We characterize transmission quality and stability by calculating the transmission quality integral, which measures the deviation of the pulse shape obtained in numerical simulations with perturbed NLS equations from the shape expected by the perturbation theory for the NLS soliton. In addition, we compare the dynamics of the soliton's amplitude and frequency obtained in the simulations with the dynamics expected by the perturbation theory. We first study soliton propagation in the absence of delayed Raman response. Our numerical simulations with the perturbed NLS equations show that transmission quality in waveguides with frequency-independent linear gain and cubic loss is comparable to transmission quality in waveguides with frequency-dependent linear gain-loss and cubic loss. We then include the effects of delayed Raman response in the perturbed NLS model. Our numerical simulations show that in waveguides with frequency-independent linear gain, cubic loss, and delayed Raman response, the soliton's

spectrum becomes separated from the radiation's spectrum due to the Raman-induced self-frequency shift experienced by the soliton. However, in this case transmission quality is not improved compared with transmission quality in the absence of delayed Raman response due to the lack of an efficient mechanism for suppression of radiation emission. Furthermore, for waveguides with frequency-dependent linear gain-loss, cubic loss, and delayed Raman response, we observe significant enhancement of transmission quality and stability compared with transmission quality and stability in the absence of delayed Raman response. The enhancement of transmission quality and stability in the latter waveguides is enabled by the separation of the soliton's spectrum from the radiation's spectrum due to the Raman self-frequency shift and by the efficient suppression of radiation emission due to the frequency-dependent linear gain-loss. Additionally, we show by further numerical simulations that enhancement of transmission quality in waveguides with frequency-dependent linear gain-loss, cubic loss, and delayed Raman response is similar to transmission quality enhancement in waveguides with weak linear gain, cubic loss, and guiding filters with a varying central frequency. More specifically, we demonstrate that the variation of the central filtering frequency leads to separation of the soliton's spectrum from the radiation's spectrum, while the presence of the guiding filters leads to efficient suppression of radiation emission. Thus, our study demonstrates a general mechanism for stabilizing soliton transmission, which is based on the interplay between frequency-dependent linear gain-loss and perturbation-induced shifting of the soliton frequency.

We choose to study pulse propagation in optical waveguides with linear gain or loss and cubic loss as a major example for waveguides, in which linear and nonlinear dissipation plays an important role in pulse dynamics. The waveguide's cubic loss can arise due to two-photon absorption (2PA) or gain-loss saturation [23–26]. Pulse propagation in the presence of 2PA or cubic loss has been studied in many previous works [12,27–36]. The subject received further attention in recent years due to the importance of 2PA in silicon nanowaveguides, which are expected to play a key role in many applications in optoelectronic devices [24,25,37,38]. These applications include modulators [39,40], switches [41,42], regeneration [43], pulse compression [44], logical gates [45,46], and supercontinuum generation [47]. In many of the applications it is desired to achieve a steady state, in which the pulse propagates along the waveguide with a constant amplitude. This can be realized by providing linear gain via Raman amplification [48–52]. However, in this case soliton propagation might become unstable since the presence of linear gain can lead to an unstable growth of small amplitude waves that are associated with radiation. It is therefore important to find ways to suppress this radiative instability. In this paper we show that the radiative instability can be suppressed by the interplay between frequency-dependent linear gain-loss and the Raman self-frequency shift.

The rest of the paper is organized as follows. In Sec. II, we study transmission stabilization in waveguides with linear gain or loss and cubic loss, considering frequency-independent linear gain in Sec. II A and frequency-dependent linear gain-loss in Sec. II B. In Sec. III, we investigate transmission stabilization in waveguides with linear gain or loss, cubic loss, and delayed Raman response. We consider frequency-independent

linear gain in Sec. III A and frequency-dependent linear gain-loss in Sec. III B. In Sec. IV, we study transmission stabilization in waveguides with linear gain, cubic loss, and guiding optical filters, considering a constant central filtering frequency in Sec. IV A and a varying central filtering frequency in Sec. IV B. Our conclusions are summarized in Sec. V. In Appendix A, we present a brief summary of the adiabatic perturbation theory for the NLS soliton. In Appendix B, we derive the equation for dynamics of the soliton's amplitude in the presence of frequency-dependent linear gain-loss, while in Appendix C, we describe the calculation of the transmission quality integral.

## II. PULSE DYNAMICS IN WAVEGUIDES WITH LINEAR GAIN-LOSS AND CUBIC LOSS

### A. Introduction

Let us give a brief summary of the results of our analytic and numerical investigation of soliton propagation in waveguides with frequency-independent linear gain and cubic loss. The value of the frequency-independent linear gain coefficient is chosen such that stable soliton transmission with a constant amplitude can be realized. More accurately, the linear gain coefficient is chosen such that according to the adiabatic perturbation theory for the NLS soliton, the soliton's amplitude value would tend to a constant predetermined value with increasing distance. However, the adiabatic perturbation theory neglects radiation emission effects. The latter effects might become important at large distances, and this might lead to pulse shape distortion and to the breakdown of the perturbation theory predictions. We therefore check the predictions of the adiabatic perturbation theory by numerical simulations with the perturbed NLS model. Our numerical simulations show that the soliton develops a radiative tail at relatively short distances, and that the radiative tail grows as the soliton continues to propagate along the waveguide. The growth of the radiative tail leads to significant reduction in transmission quality, as measured by the transmission quality integral.

Further insight into transmission quality degradation is gained by analyzing the shape of the Fourier transform of the pulse, i.e., the graph of the absolute value of the Fourier transform of the optical field vs frequency. We find that the growth of the radiative tail is manifested by a growth in the deviation of the numerically obtained shape of the Fourier transform of the pulse from the shape predicted by the adiabatic perturbation theory. This deviation appears as fast oscillations in the numerically obtained curve of the shape of the Fourier transform, which are most pronounced at small frequencies. Despite of the growth of the radiative tail and the reduction in transmission quality, we observe good agreement between the results of numerical simulations and the predictions of the adiabatic perturbation theory for dynamics of the soliton's amplitude. We attribute this good agreement to the fact that radiation emission affects the soliton's amplitude only in the second order of the small perturbation parameter, the cubic loss coefficient (see, e.g., Refs. [53,54]).

### B. Waveguides with frequency-dependent linear gain-loss and cubic loss

As explained in Sec. II A, transmission quality in a waveguide with frequency-independent linear gain and cubic loss is

degraded at relatively short distances due to radiation emission. It is therefore important to look for waveguide setups, in which radiation emission might be suppressed. A possible way for achieving this goal is by employing frequency-dependent linear gain-loss, such that the weak effects of cubic loss are balanced by weak linear gain in a frequency interval centered around the soliton frequency, while radiation emission effects are mitigated by relatively strong linear loss outside this frequency interval [16–19]. Indeed, it was shown in several recent works that the implementation of such frequency-dependent linear gain-loss can lead to significant enhancement of transmission stability in *multisequence* soliton-based optical waveguide systems [16–19]. We therefore turn to investigate soliton propagation in nonlinear optical waveguides in the presence of frequency-dependent linear gain-loss and weak cubic loss. The propagation is described by the following perturbed NLS equation [17,18]

$$i\partial_z\psi + \partial_t^2\psi + 2|\psi|^2\psi = i\mathcal{F}^{-1}(\hat{g}(\omega)\hat{\psi})/2 - i\epsilon_3|\psi|^2\psi, \quad (1)$$

where  $\psi$  is proportional to the envelope of the electric field,  $z$  is propagation distance,  $t$  is time,  $\omega$  is frequency, and  $\epsilon_3$  is the cubic loss coefficient, which satisfies  $0 < \epsilon_3 \ll 1$  [55]. In addition,  $\hat{g}(\omega)$  is the frequency-dependent linear gain-loss,  $\hat{\psi}$  is the Fourier transform of  $\psi$  with respect to time, and  $\mathcal{F}^{-1}$  is the inverse Fourier transform with respect to time. The second and third terms on the left-hand side of Eq. (1) are due to second-order dispersion and Kerr nonlinearity. The first and second terms on the right-hand side of Eq. (1) are due to frequency-dependent linear gain-loss and cubic loss. In this paper, we study transmission stabilization for fundamental solitons of the unperturbed NLS equation. The envelope of the electric field for these solitons is given by

$$\psi_s(t, z) = \eta \exp(i\chi) / \cosh(x), \quad (2)$$

where  $x = \eta(t - y + 2\beta z)$ ,  $\chi = \alpha - \beta(t - y) + (\eta^2 - \beta^2)z$ , and  $\eta$ ,  $\beta$ ,  $y$ , and  $\alpha$  are the soliton amplitude, frequency, position, and phase.

The form of  $\hat{g}(\omega)$  is chosen such that radiation emission effects are mitigated, while the value of the soliton's amplitude approaches a constant predetermined value  $\eta_0$  with increasing propagation distance. In particular, we choose the form [19]

$$\hat{g}(\omega) = -g_L + \frac{1}{2}(g_0 + g_L)[\tanh\{\rho[\omega + \beta(0) + W/2]\} - \tanh\{\rho[\omega + \beta(0) - W/2]\}], \quad (3)$$

where  $g_0$  is the linear gain coefficient,  $\beta(0)$  is the initial soliton frequency, and  $g_L$  is an  $O(1)$  positive constant. The constants  $g_0$ ,  $W$ , and  $\rho$  satisfy  $0 < g_0 \ll 1$ ,  $W \gg 1$ , and  $\rho \gg 1$ . In the limit  $\rho \gg 1$ , the linear gain-loss  $\hat{g}(\omega)$  can be approximated by a step function, which is equal to  $g_0$  inside a frequency interval of width  $W$  centered about  $-\beta(0)$ , and to  $-g_L$  elsewhere:

$$\hat{g}(\omega) \simeq \begin{cases} g_0 & \text{if } -\beta(0) - W/2 < \omega < -\beta(0) + W/2, \\ (g_0 - g_L)/2 & \text{if } \omega = -\beta(0) - W/2 \\ & \text{or } \omega = -\beta(0) + W/2, \\ -g_L & \text{elsewhere.} \end{cases} \quad (4)$$

The potential advantages of using the frequency-dependent linear gain-loss function (3) can be explained with the help of the approximate expression (4). The weak linear gain  $g_0$  in the

frequency interval  $(-\beta(0) - W/2, -\beta(0) + W/2)$  balances the effects of cubic loss, such that the soliton amplitude tends to  $\eta_0$  with increasing  $z$ . The relatively strong linear loss  $g_L$  leads to suppression of emission of radiation with frequencies outside of the interval  $(-\beta(0) - W/2, -\beta(0) + W/2)$ . The flat gain in the interval  $(-\beta(0) - W/2, -\beta(0) + W/2)$  can be realized by flat-gain amplifiers [56], and the strong loss outside of this interval can be achieved by filters [56] or by waveguide impurities [1].

The equations for the dynamics of the soliton's amplitude and frequency are obtained by using the adiabatic perturbation theory for the NLS soliton, which is described for example in Refs. [3,53,54,57] and in Appendix A. In Appendix B, we use this perturbation theory to show that the equations for the amplitude and frequency dynamics are

$$\frac{d\eta}{dz} = [-g_L + (g_0 + g_L) \tanh(V) - 4\epsilon_3 \eta^2/3] \eta, \quad (5)$$

where  $V = \pi W/(4\eta)$ , and  $d\beta/dz = 0$ , respectively. In this study, we are interested in realizing stable soliton transmission with a constant amplitude  $\eta_0 > 0$ . We therefore require that  $\eta = \eta_0 > 0$  is a stable equilibrium point of Eq. (5). This requirement yields

$$g_0 = g_L \left[ \frac{1}{\tanh(V_0)} - 1 \right] + \frac{4\epsilon_3 \eta_0^2}{3 \tanh(V_0)}, \quad (6)$$

where  $V_0 = \pi W/(4\eta_0)$ . Substituting Eq. (6) into Eq. (5), we obtain

$$\frac{d\eta}{dz} = \eta \left\{ g_L \left[ \frac{\tanh(V)}{\tanh(V_0)} - 1 \right] + \frac{4}{3} \epsilon_3 \left[ \eta_0^2 \frac{\tanh(V)}{\tanh(V_0)} - \eta^2 \right] \right\}. \quad (7)$$

In Appendix B, we show that the only equilibrium points of Eq. (7) with  $\eta \geq 0$  are  $\eta = \eta_0$  and  $\eta = 0$ . In addition, we show that  $\eta = \eta_0$  is a stable equilibrium point, while  $\eta = 0$  is an unstable equilibrium point.

*Comparison with amplitude dynamics in waveguides with linear gain and cubic loss.* It can be shown by the adiabatic perturbation theory that the equations for amplitude and frequency dynamics for soliton propagation in a nonlinear optical waveguide with frequency-independent linear gain and cubic loss are

$$\frac{d\eta}{dz} = \frac{4}{3} \epsilon_3 \eta (\eta_0^2 - \eta^2) \quad (8)$$

and  $d\beta/dz = 0$ , respectively. The solution of Eq. (8) for a soliton with an initial amplitude  $\eta(0)$  is

$$\eta(z) = \eta_0 \left[ 1 + \left( \frac{\eta_0^2}{\eta^2(0)} - 1 \right) \exp(-8\eta_0^2 \epsilon_3 z/3) \right]^{-\frac{1}{2}}. \quad (9)$$

Equation (8) has two equilibrium points with non-negative amplitude values at  $\eta = \eta_0$  and at 0, where  $\eta = \eta_0$  is stable and  $\eta = 0$  is unstable. Thus, the replacement of frequency-independent linear gain by frequency-dependent linear gain-loss does not change the number, locations, and stability properties of the equilibrium points. We also note that in the typical transmission setup that we consider in this work,  $\eta_0$  is of order 1,  $\eta$  is of order 1 or smaller, and  $W \gg 1$  [58]. Therefore, in this case both  $V_0$  and  $V$  satisfy  $V_0 \gg 1$  and  $V \gg 1$ , and one can obtain an approximate form of Eq. (7) by expanding its

right-hand side in a Taylor series with respect to  $e^{-2V_0}$  and  $e^{-2V}$ . Keeping terms up to first order in the expansion, we obtain

$$\frac{d\eta}{dz} = \left[ 2g_L(e^{-2V_0} - e^{-2V}) + \frac{4}{3} \epsilon_3 (\eta_0^2 - \eta^2) + \frac{8}{3} \epsilon_3 \eta_0^2 (e^{-2V_0} - e^{-2V}) \right] \eta. \quad (10)$$

Comparing Eq. (10) with Eq. (8) we see that in the typical transmission setup, the correction terms that appear in the equation for amplitude dynamics due to the introduction of frequency-dependent linear gain-loss are exponentially small in both  $V_0$  and  $V$ .

*Numerical simulations.* The prediction for stable dynamics of the soliton amplitude that was obtained in the previous paragraph was based on an adiabatic perturbation description, which neglects the effects of radiation emission. However, radiation emission effects can become significant at large propagation distances and this can lead to pulse shape distortion and to the breakdown of the adiabatic perturbation description of Eq. (7). This is especially true in waveguides with linear gain since the presence of linear gain leads to unstable growth of small amplitude waves that are associated with radiation. It is therefore important to check the predictions of the adiabatic perturbation theory by numerical simulations with the perturbed NLS model (1) with the linear gain-loss (3).

Equation (1) is numerically solved on a domain  $[t_{\min}, t_{\max}] = [-1600, 1600]$  using the split-step method with periodic boundary conditions [1,59]. The initial condition is in the form of a single NLS soliton  $\psi_s$  with amplitude  $\eta(0)$ , frequency  $\beta(0) = 0$ , position  $y(0) = 0$ , and phase  $\alpha(0) = 0$ . For concreteness, we present here the results of numerical simulations with  $\epsilon_3 = 0.01$  and  $\eta(0) = 0.8$ . In addition, the values of the parameters  $W$ ,  $\rho$ , and  $g_L$  of the frequency-dependent linear gain-loss  $\hat{g}(\omega)$  are similar to the values used in Refs. [16–19] in studies of multisequence soliton-based transmission:  $W = 10$ ,  $\rho = 10$ , and  $g_L = 0.5$ . These values were found to lead to enhanced stability of soliton propagation in multisequence transmission systems [16–19]. We emphasize, however, that similar results are obtained for other physical parameter values. To avoid dealing with effects due to radiation leaving the computational domain at one boundary and reentering it at the other boundary, we employ damping near the domain boundaries. The same method for suppressing reentry of radiation into the computational domain was successfully used in many earlier studies of pulse propagation in nonlinear optical waveguides (see, e.g., Refs. [35,60,61]). Physically, the damping at the boundaries can be realized by employing filters at the waveguide ends [1,2]. Thus, the numerical simulations in the current section correspond to transmission in an open optical waveguide.

Transmission quality at a distance  $z$  is measured from the results of the numerical simulations by calculating the transmission quality integral  $I(z)$  in Eq. (C4) in Appendix C. This integral measures the deviation of the numerically obtained pulse shape  $|\psi^{(\text{num})}(t, z)|$  from the soliton's shape expected by the adiabatic perturbation theory  $|\psi^{(\text{th})}(t, z)|$ , which is given by Eq. (C1). Thus,  $I(z)$  measures both distortion in the pulse shape due to radiation emission and deviations of the numerically obtained values of the soliton's parameters

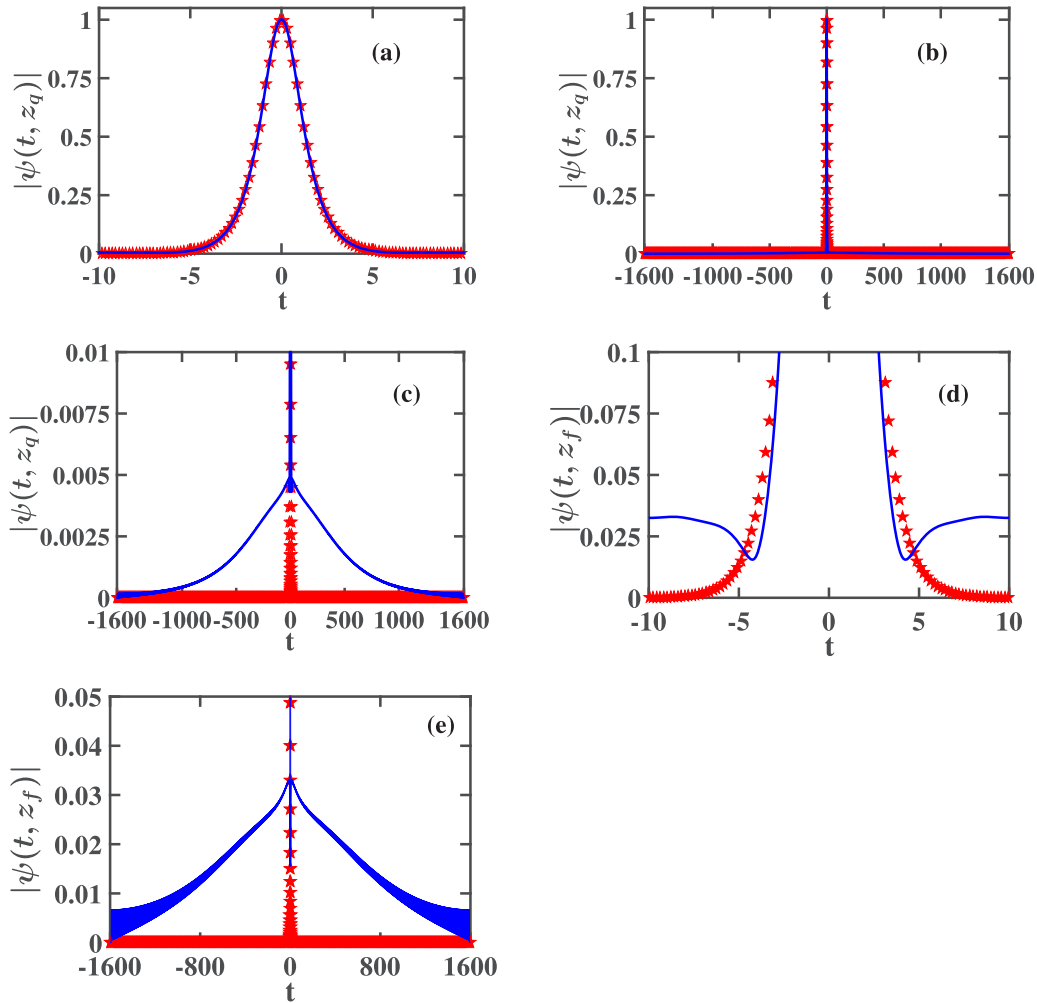


FIG. 1. The pulse shape  $|\psi(t, z)|$  at  $z_q = 432$  [(a)–(c)] and at  $z_f = 750$  [(d), (e)] for soliton propagation in an open optical waveguide with weak frequency-dependent linear gain-loss and cubic loss. The cubic loss coefficient is  $\epsilon_3 = 0.01$ , the initial soliton amplitude is  $\eta(0) = 0.8$ , and the parameters of the linear gain-loss  $\hat{g}(\omega)$  in Eq. (3) are  $W = 10$ ,  $\rho = 10$ , and  $g_L = 0.5$ . The solid blue curve corresponds to the result obtained by numerical simulations with Eqs. (1) and (3), while the red stars correspond to the prediction of the perturbation theory, obtained with Eqs. (C1) and (7).

from the values predicted by the adiabatic perturbation theory. Transmission quality is further quantified by measuring the transmission quality distance  $z_q$ , which is the distance at which the value of  $I(z)$  first exceeds 0.075. To characterize pulse shape degradation at larger distances, we run the simulation up to a final propagation distance  $z_f$  at which the value of  $I(z)$  first exceeds 0.655. In the numerical simulation with the physical parameter values specified in the preceding paragraph, we find  $z_q = 432$  and  $z_f = 750$ . We note that these values of  $z_q$  and  $z_f$  are the same as the values obtained in numerical simulations for soliton propagation in waveguides with frequency-independent linear gain and cubic loss.

The pulse shape  $|\psi(t, z)|$  obtained in the simulations at  $z = z_q$  and at  $z = z_f$  is shown in Fig. 1. Also shown is the prediction of the adiabatic perturbation theory, obtained with Eqs. (C1) and (7). As seen in Figs. 1(a) and 1(b), the pulse shape obtained by the simulations at  $z = z_q$  is close to the analytic prediction. However, the comparison of the analytic prediction with the numerical result for small  $|\psi(t, z_q)|$  values in Fig. 1(c) reveals that an appreciable radiative tail exists already at  $z = z_q$ .

As the soliton continues to propagate along the waveguide, the radiative tail continues to grow [see Figs. 1(d) and 1(e)]. The growth of the radiative tail is also manifested in Fig. 2,

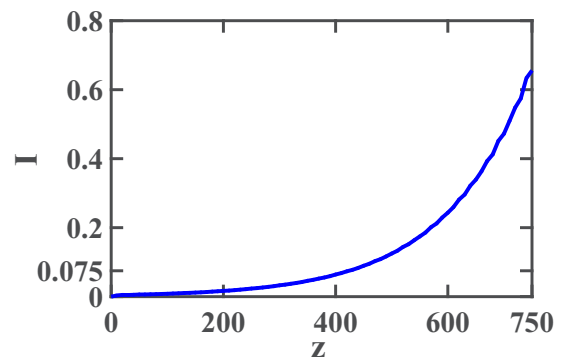


FIG. 2. The  $z$  dependence of the transmission quality integral  $I(z)$  obtained by numerical simulations with Eqs. (1) and (3) for the same optical waveguide setup considered in Fig. 1.

which shows the values of the integral  $I(z)$  obtained in the simulations. As seen in this figure, the value of  $I(z)$  increases from 0.075 at  $z_q = 432$  to 0.6557 at  $z_f = 750$ . We point out that pulse shape degradation observed in Fig. 1 is very similar to pulse shape degradation observed for soliton propagation in waveguides with frequency-independent linear gain and cubic loss. As a result, the values of  $I(z)$  obtained in the two waveguide systems are also very close. Therefore, the replacement of frequency-independent linear gain by frequency-dependent linear gain-loss does not lead to enhancement of transmission quality.

The growth of the radiative tail can be further characterized by the shape of the Fourier transform of the pulse  $|\hat{\psi}(\omega, z)|$ . Figure 3 shows the numerically obtained  $|\hat{\psi}(\omega, z)|$  at  $z = z_q$  and at  $z = z_f$  along with the prediction of the adiabatic perturbation theory, obtained with Eqs. (C3) and (7). As seen in Figs. 3(a) and 3(b), the deviation of the numerical result from the analytic prediction is noticeable already at  $z = z_q$ . This deviation appears as fast oscillations in the numerical curve of  $|\hat{\psi}(\omega, z)|$  vs  $\omega$ , which are most pronounced near  $\omega = 0$ , i.e., at relatively small frequencies. Since the deviation appears as distortion in the shape of the Fourier transform of the pulse, it is associated with the radiative tail. Furthermore, we observe that the deviation of the numerical result from the analytic prediction continues to grow as the pulse continues to propagate along the waveguide and is of order 1 at  $z = z_f$  [see Fig. 3(c)]. We note that the numerically obtained graphs of  $|\hat{\psi}(\omega, z_q)|$  and  $|\hat{\psi}(\omega, z_f)|$  vs  $\omega$  are very similar to the graphs obtained for waveguides with frequency-independent linear gain and cubic loss. In particular, for both waveguide systems, the graphs contain fast oscillations at small frequencies, which are associated with the existence of a radiative tail. These findings can be explained by noting the lack of observable separation between the Fourier spectrum of the soliton and the Fourier spectrum of the radiation in Fig. 3. As a result, the introduction of the frequency-dependent linear gain-loss with  $W$  values satisfying  $W \gg 1$  does not lead to efficient mitigation of radiation emission. Thus, transmission quality in waveguides with frequency-dependent linear gain-loss and cubic loss is very close to transmission quality in waveguides with frequency-independent linear gain and cubic loss. We will demonstrate in Secs. III B and IV B that the situation changes dramatically due to the effects of delayed Raman response or due to the effects of guiding optical filters with a varying central frequency.

Figure 4 shows the  $z$  dependence of the soliton's amplitude obtained in the simulations together with the analytic prediction of Eq. (7). We observe good agreement between the numerical and analytic results for  $0 \leq z \leq 600$ , while for  $600 < z \leq 750$ , the difference between the numerical result and the analytic prediction becomes noticeable. Thus, the dynamics of the soliton's amplitude is still stable in the interval  $0 \leq z \leq 750$ . Similar dynamics of the soliton's amplitude is observed for waveguides with frequency-independent linear gain and cubic loss. The good agreement between the prediction of the adiabatic perturbation theory and the numerical result for  $\eta(z)$  can be attributed to the fact that radiation emission affects the dynamics of  $\eta$  only in second order of the small perturbation parameter  $\epsilon_3$  (see, e.g., Refs. [53,54]).

We emphasize that the effects of radiation emission due to weak perturbations can have much stronger impact on

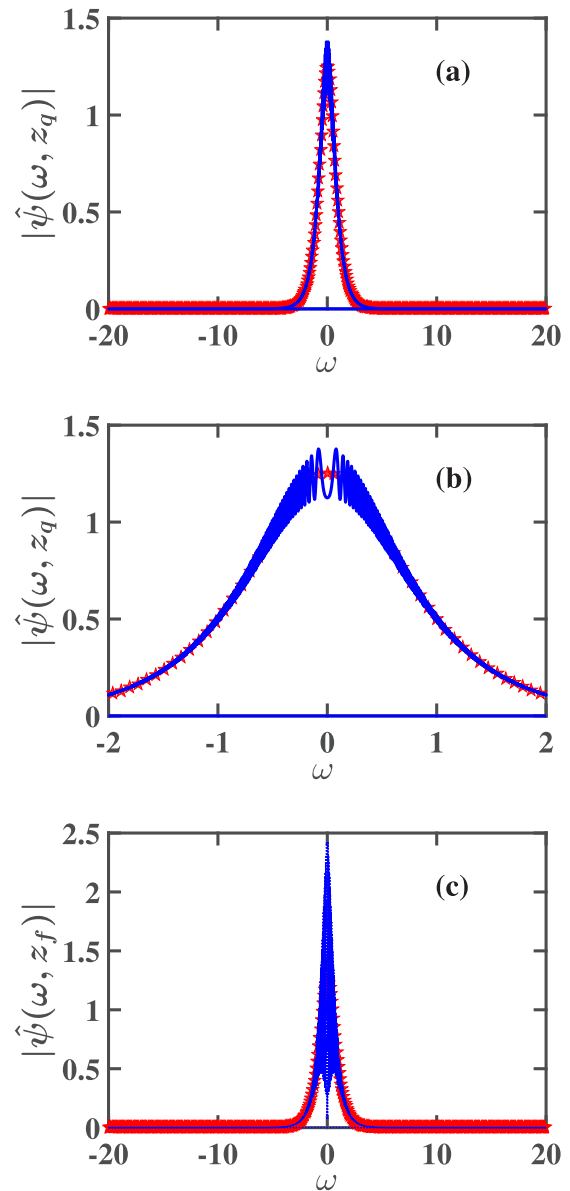


FIG. 3. The Fourier transform of the pulse shape  $|\hat{\psi}(\omega, z)|$  at  $z_q = 432$  [(a), (b)] and at  $z_f = 750$  (c) for soliton propagation in an open optical waveguide with weak frequency-dependent linear gain-loss and cubic loss. The physical parameter values are the same as in Fig. 1. The solid blue curve represents the result obtained by numerical simulations with Eqs. (1) and (3), while the red stars correspond to the prediction of the adiabatic perturbation theory, obtained with Eqs. (C3) and (7).

soliton dynamics and stability compared with the impact observed here for single-soliton propagation in an open optical waveguide. More specifically, in the case of transmission of a soliton sequence through an optical waveguide, the emitted radiation leads to long-range interaction between the solitons, which in turn leads to the breakup of the soliton pattern [54]. Furthermore, in the case of transmission of multiple soliton sequences through an optical waveguide, the radiation emitted by the solitons in a given sequence can resonantly interact with solitons from other sequences [16,17,19]. This resonant interaction leads to severe pulse pattern distortion

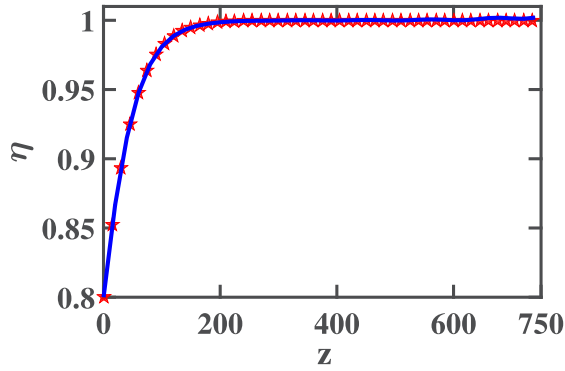


FIG. 4. The  $z$  dependence of the soliton amplitude  $\eta(z)$  for the open waveguide setup considered in Figs. 1–3. The solid blue curve represents the result obtained by numerical simulations with Eqs. (1) and (3). The red stars represent the perturbation theory prediction of Eq. (7).

and eventually to the destruction of the soliton sequences [12,13,16,17,19]. Finally, in the case of a soliton propagating in a closed waveguide loop, the accumulation of the emitted radiation and its interaction with the soliton will also lead to pulse shape distortion and to the destruction of the soliton. This latter scenario will be discussed and demonstrated in Sec. III A.

### III. PULSE DYNAMICS IN WAVEGUIDES WITH LINEAR GAIN-LOSS, CUBIC LOSS, AND DELAYED RAMAN RESPONSE

*Introduction.* As seen in Sec. II B, the replacement of frequency-independent linear gain by frequency-dependent linear gain-loss does not lead to significant enhancement of transmission quality. On the other hand, numerical simulations of multisequence soliton-based transmission show that transmission stability is significantly enhanced when the effects of delayed Raman response and frequency-dependent linear gain-loss are both taken into account [16,17]. It is therefore important to investigate whether the presence of delayed Raman response can improve transmission quality in the single-soliton propagation problem considered in this paper. We now turn to address this question.

#### A. Waveguides with frequency-independent linear gain, cubic loss, and delayed Raman response

We start by considering the impact of delayed Raman response on the propagation of a single soliton in nonlinear optical waveguides with weak frequency-independent linear gain and cubic loss. The propagation is described by the following perturbed NLS equation [24,25]

$$\begin{aligned} i\partial_z\psi + \partial_t^2\psi + 2|\psi|^2\psi \\ = ig_0\psi/2 - i\epsilon_3|\psi|^2\psi + \epsilon_R\psi\partial_t|\psi|^2, \end{aligned} \quad (11)$$

where the Raman coefficient  $\epsilon_R$  satisfies  $0 < \epsilon_R \ll 1$  [62,63]. The third term on the right-hand side of Eq. (11) describes the effects of delayed Raman response.

A calculation based on the adiabatic perturbation theory shows that the main effect of delayed Raman response on single-soliton propagation is a frequency shift, whose rate is

given by [20–22]

$$\frac{d\beta}{dz} = -\frac{8}{15}\epsilon_R\eta^4. \quad (12)$$

The soliton amplitude is not affected by delayed Raman response in  $O(\epsilon_R)$  [20–22]. Therefore, the dynamics of the soliton amplitude is still given by Eqs. (8) and (9). Substituting  $\eta(z)$  from Eq. (9) into Eq. (12) and integrating with respect to  $z$ , we obtain

$$\begin{aligned} \beta(z) = \beta(0) - \frac{\epsilon_R\eta_0^2}{5\epsilon_3} \\ \times \left\{ \ln \left[ \frac{\eta_0^2 - \eta^2(0) + \eta^2(0) \exp(8\epsilon_3\eta_0^2z/3)}{\eta_0^2} \right] + \frac{\eta^2(0)}{\eta_0^2} \right. \\ \left. - \frac{\eta^2(0)}{\eta^2(0) + [\eta_0^2 - \eta^2(0)] \exp(-8\epsilon_3\eta_0^2z/3)} \right\}. \end{aligned} \quad (13)$$

The soliton position and phase are affected by the perturbations only via the dependence of  $\eta$  and  $\beta$  on  $z$ .

*Numerical simulations.* Equation (11) is numerically solved on a domain  $[t_{\min}, t_{\max}] = [-400, 400]$  with periodic boundary conditions. The initial condition is in the form of a single NLS soliton with amplitude  $\eta(0)$ , frequency  $\beta(0) = 0$ , position  $y(0) = 0$ , and phase  $\alpha(0) = 0$ . As a typical example, we present here the results of the simulations with  $\epsilon_3 = 0.01$ ,  $\epsilon_R = 0.04$ , and  $\eta(0) = 0.8$ . We point out that similar results are obtained for other physical parameter values. Due to the presence of delayed Raman response and the relatively large propagation distance, the soliton experiences a very large position shift. For example, for  $\epsilon_R = 0.04$ ,  $\eta(0) = 1$ , and  $\tilde{z} = 750$ , we find using the adiabatic perturbation theory that the soliton position shift at  $\tilde{z} = 750$  is  $y(\tilde{z}) = 8\epsilon_R\eta^4(0)\tilde{z}^2/15 = 12000$ . Carrying out numerical simulations for transmission in an open optical waveguide setup, i.e., in a setup in which the soliton does not reach the computational domain's boundaries, is prohibitively time consuming since one has to employ a computational domain with a size exceeding 12000. We therefore choose to work with a numerical simulations setup, in which the soliton passes through the computational domain's boundaries multiple times during the simulation. In such setup, we do *not* use damping at the boundaries since such damping leads to the soliton's destruction. Note that the numerical simulations setup used in the current section corresponds to soliton propagation in a closed optical waveguide loop. This setup is very relevant for applications since many long-distance transmission experiments are carried out in closed waveguide loops (see, e.g., Refs. [2,5–10] and references therein). The values of the transmission quality distance and the final propagation distance obtained in the simulations were  $z_q = 378$  and  $z_f = 785$ .

Figure 5 shows the pulse shape  $|\psi(t, z)|$  at  $z = z_q$  and at  $z_f$ , obtained in the simulations together with the prediction of the adiabatic perturbation theory, obtained with Eqs. (C1) and (9). As seen in Figs. 5(a)–5(c), the numerically obtained pulse shape at  $z = z_q$  is close to the analytic prediction, although, a noticeable radiative tail exists at this distance. We observe that the radiative tail is highly oscillatory and is spread over the entire computational domain at  $z = z_q$ . The oscillatory nature of the radiative tail is attributed to the presence of

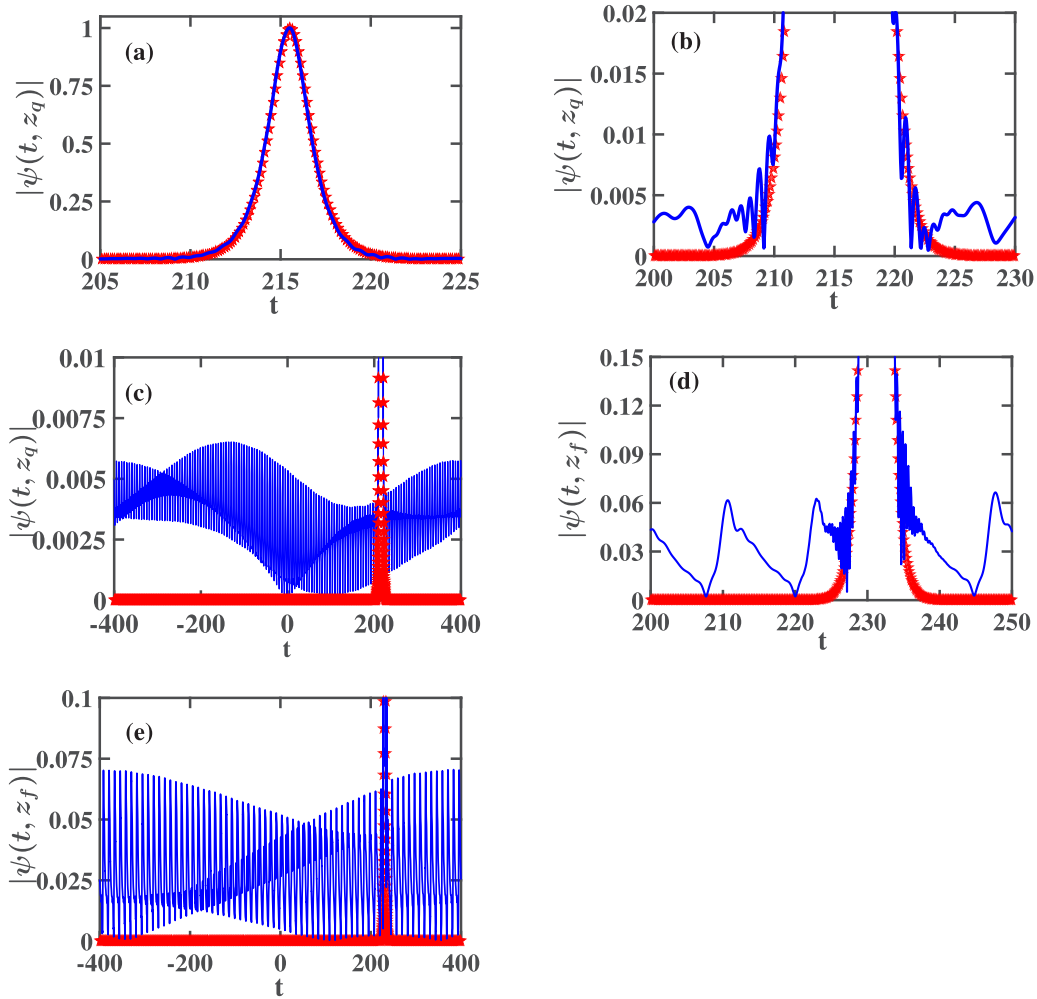


FIG. 5. The pulse shape  $|\psi(t, z)|$  at  $z_q = 378$  [(a)–(c)] and at  $z_f = 785$  [(d), (e)] for soliton propagation in a closed optical waveguide loop with weak frequency-independent linear gain, cubic loss, and delayed Raman response. The cubic loss coefficient is  $\epsilon_3 = 0.01$ , the Raman coefficient is  $\epsilon_R = 0.04$ , and the initial soliton amplitude is  $\eta(0) = 0.8$ . The solid blue curve corresponds to the result obtained by numerical simulations with Eq. (11), while the red stars correspond to the perturbation theory prediction of Eqs. (C1) and (9).

delayed Raman response. The spread of radiation over the entire computational domain is due to additional emission of radiation induced by the presence of delayed Raman response, the closed waveguide loop setup, which leads to accumulation of radiation, and the smaller size of the computational time domain compared with the one used in the simulations in Sec. II. We also observe that the radiative tail continues to grow as the soliton continues to propagate along the waveguide [see Figs. 5(d) and 5(e)]. As a result, the value of the transmission quality integral  $I(z)$  increases from 0.075 at  $z_q = 378$  to 0.6565 at  $z_f = 785$  (see Fig. 6).

Further insight into transmission quality degradation and pulse dynamics is gained from the shape of the Fourier spectrum  $|\hat{\psi}(\omega, z)|$ . Figure 7 shows the numerically obtained  $|\hat{\psi}(\omega, z)|$  at  $z = z_q$  and at  $z_f$  together with the prediction of the adiabatic perturbation theory, obtained with Eqs. (C3), (9), and (13). It is clear that the Fourier spectrum of the optical field for waveguides with frequency-independent linear gain, cubic loss, and delayed Raman response is very different from the Fourier spectrum observed in Sec. II for soliton propagation in the absence of delayed Raman response. More specifically,

the soliton's Fourier spectrum in the current waveguide setup is centered about the nonzero  $z$ -dependent soliton's frequency  $\beta(z)$  and is shifted relative to the radiation's spectrum, which is centered near  $\omega = 0$ . The separation between the soliton's

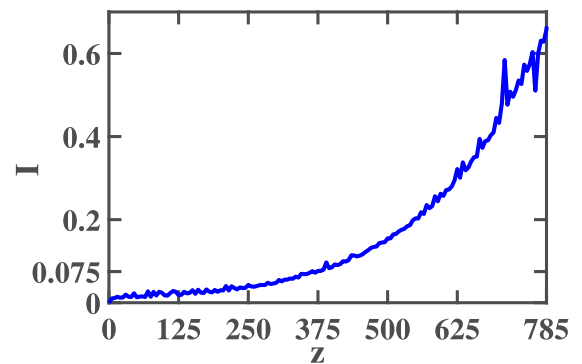


FIG. 6. The  $z$  dependence of the transmission quality integral  $I(z)$  obtained by numerical simulations with Eq. (11) for the same optical waveguide setup considered in Fig. 5.



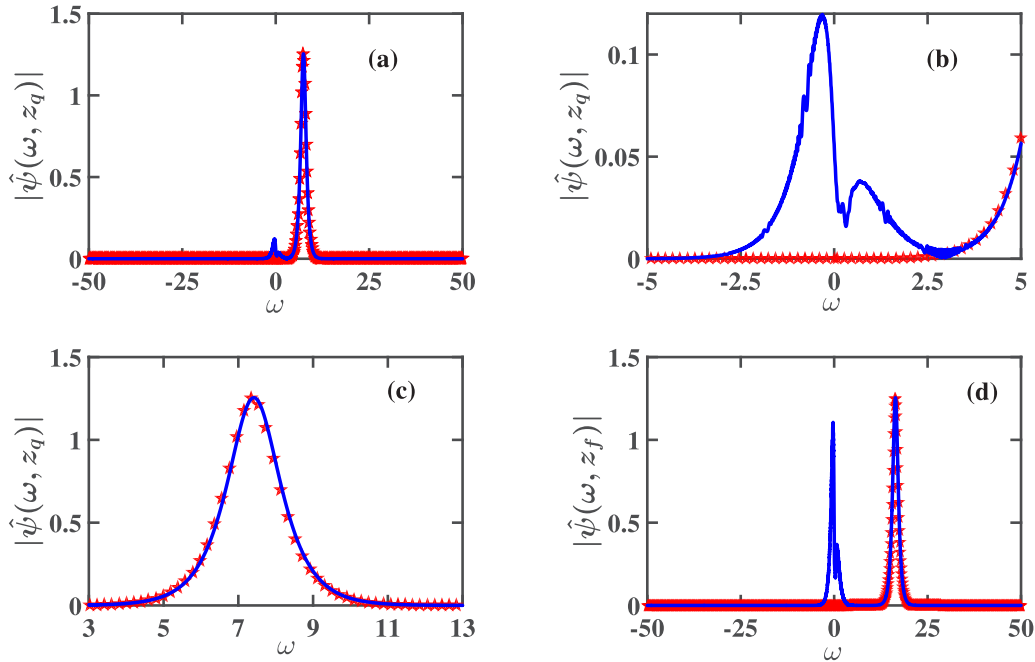


FIG. 7. The Fourier transform of the pulse shape  $|\hat{\psi}(\omega, z)|$  at  $z_q = 378$  [(a)–(c)] and at  $z_f = 785$  (d) for soliton propagation in a closed optical waveguide loop with weak frequency-independent linear gain, cubic loss, and delayed Raman response. The physical parameter values are the same as in Fig. 5. The solid blue curve represents the result obtained by numerical simulations with Eq. (11) and the red stars correspond to the prediction of the adiabatic perturbation theory, obtained with Eqs. (C3), (9), and (13).

spectrum and the radiation's spectrum, which is a result of the Raman self-frequency shift experienced by the soliton, is already very clear at  $z = z_q$  [see Figs. 7(a) and 7(b)]. It continues to grow with increasing  $z$  due to the increase in  $|\beta(z)|$  [see Fig. 7(d)]. As a result of the separation between the two spectra, the soliton part of the numerically obtained graph of  $|\hat{\psi}(\omega, z)|$  does not contain fast oscillations and is very close to the prediction of the adiabatic perturbation theory [see Fig. 7(c)]. In contrast, in the waveguides considered in Sec. II, the Fourier spectrum of the entire optical field (soliton + radiation) is centered about  $\omega = 0$ . That is, there is no significant separation between the soliton and the radiation spectra. Therefore, for the waveguides considered in Sec. II, the deviation of the numerically obtained Fourier spectrum from the spectrum expected for an NLS soliton is significant already at  $z = z_q$ .

The  $z$  dependence of the soliton's amplitude and frequency obtained in the simulations is shown in Figs. 8(a) and 8(b). Also shown are the adiabatic perturbation theory predictions for  $\eta(z)$  and  $\beta(z)$ , which are given by Eqs. (9) and (13), respectively. In both graphs we observe good agreement between the numerical and analytic results for  $0 \leq z \leq 500$ , whereas for  $500 < z \leq 785$ , the difference between the two results becomes significant. Based on this comparison, we conclude that the dynamics of soliton amplitude and frequency becomes unstable for distances larger than 500. We notice that the deviation of the numerical result from the analytic result for  $\eta(z)$  in the current waveguide setup is larger compared with the deviation found for soliton propagation in the absence of delayed Raman response in Sec. II. We attribute this larger deviation to the presence of a larger radiative tail [compare Fig. 5(e) with Fig. 1(e)]. The radiative tail in the current waveguide setup is larger compared with the radiative tail in

the waveguide setups of Sec. II due to additional emission of radiation induced by the presence of delayed Raman response, the closed waveguide loop setup, which leads to accumulation of radiation, and the smaller size of the computational time domain used in the simulations.

### B. Waveguides with frequency-dependent linear gain-loss, cubic loss, and delayed Raman response

We saw in Sec. III A that the presence of delayed Raman response in optical waveguides with frequency-independent linear gain and cubic loss leads to strong separation of the soliton's Fourier spectrum from the radiation's Fourier spectrum. Thus, we expect that the replacement of the frequency-independent linear gain by frequency-dependent linear gain-loss of a form similar to the one in Eq. (3) will lead to efficient suppression of radiation emission and to significant enhancement of transmission quality. We therefore turn to investigate soliton propagation in nonlinear optical waveguides in the presence of weak frequency-dependent linear gain-loss, cubic loss, and delayed Raman response. The propagation is described by the following perturbed NLS equation [16,17]:

$$i \partial_z \psi + \partial_t^2 \psi + 2|\psi|^2 \psi = i \mathcal{F}^{-1}(\hat{g}(\omega, z) \hat{\psi})/2 - i \epsilon_3 |\psi|^2 \psi + \epsilon_R \psi \partial_t |\psi|^2. \quad (14)$$

The form of the frequency- and distance-dependent linear gain-loss  $\hat{g}(\omega, z)$  is similar to the one in Eq. (3), apart from a replacement of the initial soliton frequency  $\beta(0)$  by the  $z$ -dependent soliton frequency  $\beta(z)$ . Thus,  $\hat{g}(\omega, z)$  is given by

$$\hat{g}(\omega, z) = -g_L + \frac{1}{2}(g_0 + g_L) [\tanh\{\rho[\omega + \beta(z) + W/2]\} - \tanh\{\rho[\omega + \beta(z) - W/2]\}]. \quad (15)$$

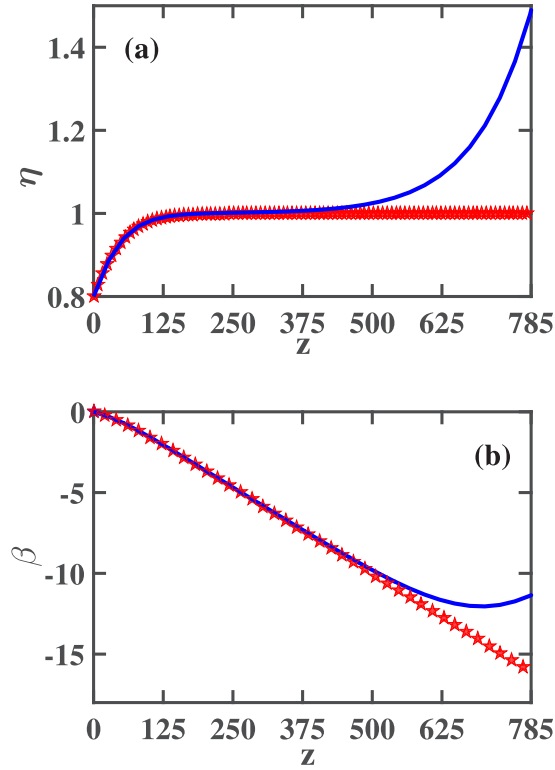


FIG. 8. The  $z$  dependence of the soliton amplitude  $\eta(z)$  (a) and frequency  $\beta(z)$  (b) for the closed optical waveguide loop setup considered in Figs. 5–7. The solid blue curves represent the results obtained by numerical simulations with Eq. (11). The red stars correspond to the perturbation theory predictions of Eq. (9) in (a) and of Eq. (13) in (b).

A similar form was used in Refs. [16,17] in studies of multisequence soliton-based transmission in the presence of delayed Raman response and different transmission stabilizing mechanisms based on frequency-dependent gain-loss. In the limit  $\rho \gg 1$ ,  $\hat{g}(\omega, z)$  can be approximated by the following step function:

$$\hat{g}(\omega, z) \simeq \begin{cases} g_0 & \text{if } -\beta(z) - W/2 < \omega < -\beta(z) + W/2, \\ (g_0 - g_L)/2 & \text{if } \omega = -\beta(z) - W/2 \\ & \text{or } \omega = -\beta(z) + W/2, \\ -g_L & \text{elsewhere.} \end{cases} \quad (16)$$

We observe that the weak linear gain  $g_0$  in the frequency interval  $(-\beta(z) - W/2, -\beta(z) + W/2)$  balances the effects of cubic loss, such that the soliton amplitude approaches the equilibrium value  $\eta_0$  with increasing  $z$ . Additionally, the relatively strong linear loss  $g_L$  leads to suppression of emission of radiation with frequencies outside of the interval  $(-\beta(z) - W/2, -\beta(z) + W/2)$ . Thus, due to the relatively large separation between the soliton's spectrum and the radiation's spectrum expected for the current waveguide setup, the introduction of the frequency-dependent linear gain-loss  $\hat{g}(\omega, z)$  of Eq. (15) is expected to lead to efficient suppression of radiation emission and to significant enhancement of transmission quality.

Since the soliton amplitude is not affected by delayed Raman response in  $O(\epsilon_R)$ , the dynamics of the amplitude is still described by Eq. (7). In addition, the dynamics of the soliton frequency is given by Eq. (12). The soliton position and phase are affected by the perturbations only via the dependence of  $\eta$  and  $\beta$  on  $z$ .

*Numerical simulations.* To check whether the interplay between frequency-dependent linear gain-loss and delayed Raman response leads to enhanced transmission quality, we perform numerical simulations with Eqs. (14) and (15). The equations are numerically integrated on a domain  $[t_{\min}, t_{\max}] = [-400, 400]$  with periodic boundary conditions. The initial condition is in the form of a single NLS soliton with amplitude  $\eta(0)$ , frequency  $\beta(0) = 0$ , position  $y(0) = 0$ , and phase  $\alpha(0) = 0$ . To enable comparison with the results of the numerical simulations in Secs. II and III A, we use the same parameter values that were used in those sections. That is, we carry out the simulations with  $\epsilon_3 = 0.01$ ,  $\epsilon_R = 0.04$ ,  $\eta(0) = 0.8$ ,  $W = 10$ ,  $\rho = 10$ , and  $g_L = 0.5$ . We emphasize, however, that similar results are obtained for other physical parameter values. Similar to the simulations in Sec. III A, the soliton passes multiple times through the computational domain's boundaries during the simulation, i.e., the simulation describes soliton propagation in a closed waveguide loop. To avoid soliton destruction, we do not employ damping at the boundaries. The simulation is run up to a predetermined final propagation distance  $z_f = 2000$ , at which the value of the transmission quality integral is still smaller than 0.075.

Figure 9 shows the pulse shape  $|\psi(t, z)|$  at  $z = z_f$ , as obtained in the simulations. The prediction of the adiabatic perturbation theory, obtained with Eqs. (C1) and (7), is also shown. As seen in Figs. 9(a) and 9(b), the numerically obtained pulse shape at  $z = z_f$  is very close to the analytic prediction and no significant radiative tail is observed. Moreover, as seen in Fig. 9(c), the deviation of the numerical result for  $|\psi(t, z_f)|$  from the theoretical one is smaller than  $10^{-6}$  for all  $t$  values. Thus, the interplay between frequency-dependent linear gain-loss and delayed Raman response does lead to significant enhancement of transmission quality compared with the waveguide setups considered in Secs. II and III A. The enhancement of transmission quality is also demonstrated in Fig. 10 that shows the numerically obtained  $I(z)$  curve and the average  $\langle I(z) \rangle$ , which is defined by  $\langle I(z) \rangle \equiv \int_0^{z_f} dz' I(z')/z_f$ . As seen in this figure, the value of  $I(z)$  remains smaller than 0.032 throughout the propagation and  $\langle I(z) \rangle = 0.0156$ .

The enhanced transmission quality can be explained with the help of the Fourier transform of the pulse  $|\hat{\psi}(\omega, z)|$ . Figure 11 shows the numerically obtained Fourier transform  $|\hat{\psi}(\omega, z)|$  at  $z = z_f$  together with the prediction of the adiabatic perturbation theory, obtained with Eqs. (C3), (7), and (12). We observe very good agreement between the two results. More specifically, in both curves, the Fourier spectrum of the soliton is strongly downshifted and is centered about the frequency  $\omega_m = -\beta(z_f) = 42.0$ . Additionally, the numerically obtained curve of  $|\hat{\psi}(\omega, z_f)|$  does not contain any fast oscillations in the main peak such as the oscillations seen in Fig. 3 (in Sec. II B) for soliton propagation in the absence of delayed Raman response. Furthermore, the numerically obtained curve of  $|\hat{\psi}(\omega, z_f)|$  does not contain any significant “radiation peaks” such as the one seen in Fig. 7 (in Sec. III A) for waveguides with

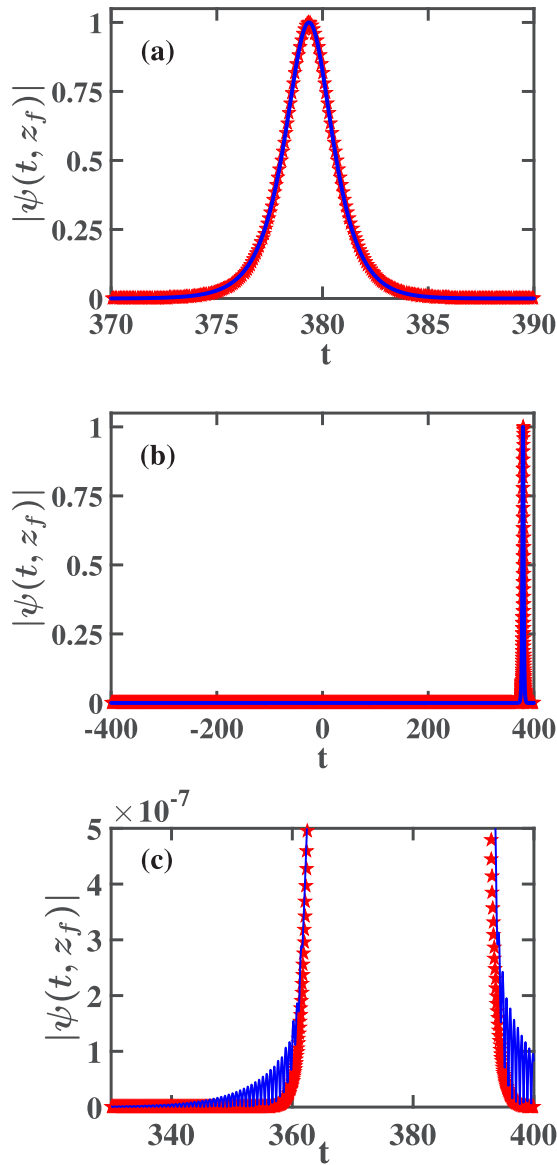


FIG. 9. The pulse shape  $|\psi(t, z_f)|$ , where  $z_f = 2000$ , for soliton propagation in a closed optical waveguide loop with weak frequency-dependent linear gain-loss, cubic loss, and delayed Raman response. The cubic loss coefficient is  $\epsilon_3 = 0.01$ , the Raman coefficient is  $\epsilon_R = 0.04$ , the initial soliton amplitude is  $\eta(0) = 0.8$ , and the parameters of the linear gain-loss  $\hat{g}(\omega, z)$  in Eq. (15) are  $W = 10$ ,  $\rho = 10$ , and  $g_L = 0.5$ . The solid blue curve corresponds to the result obtained by numerical simulations with Eqs. (14) and (15). The red stars correspond to the prediction of the adiabatic perturbation theory, obtained with Eqs. (C1) and (7).

frequency-independent linear gain, cubic loss, and delayed Raman response. Based on these observations, we conclude that the presence of delayed Raman response leads to separation of the soliton's spectrum from the radiation's spectrum via the soliton self-frequency shift, while the frequency-dependent linear gain-loss leads to efficient suppression of radiation emission. As a result, transmission quality is significantly enhanced in waveguides with frequency-dependent linear gain-loss, cubic loss, and delayed Raman response compared with the waveguide setups considered in Secs. II and III A.

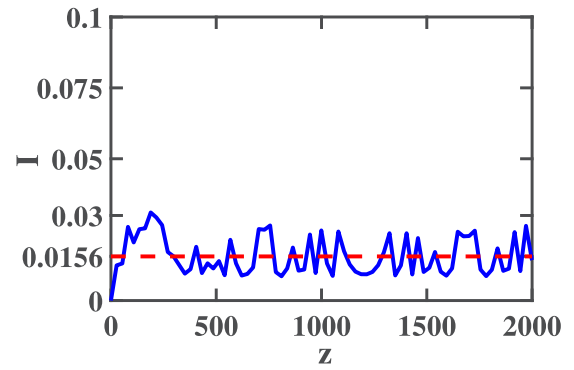


FIG. 10. The  $z$  dependence of the transmission quality integral  $I(z)$  obtained by numerical simulations with Eqs. (14) and (15) for the same optical waveguide setup considered in Fig. 9. The solid blue curve represents  $I(z)$  and the dashed red horizontal line corresponds to  $\langle I(z) \rangle$ .

The enhancement of transmission quality in waveguides with frequency-dependent linear gain-loss, cubic loss, and delayed Raman response is also manifested in the dynamics of the soliton's amplitude and frequency. Figures 12(a) and 12(b) show the  $z$  dependence of the soliton's amplitude and frequency obtained in the simulations. Also shown are the

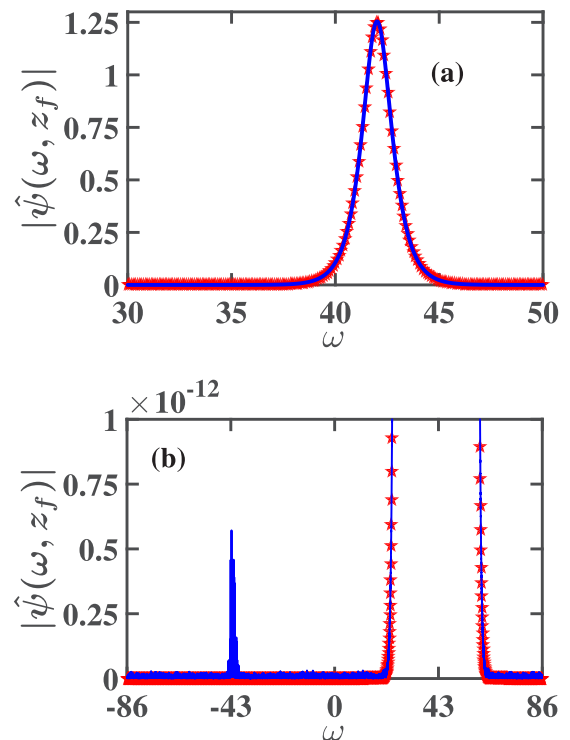


FIG. 11. The Fourier transform of the pulse shape  $|\hat{\psi}(\omega, z)|$  at  $z_f = 2000$  for soliton propagation in a closed optical waveguide loop with weak frequency-dependent linear gain-loss, cubic loss, and delayed Raman response. The physical parameter values are the same as in Fig. 9. The solid blue curve represents the result obtained by numerical simulations with Eqs. (14) and (15). The red stars correspond to the prediction of the adiabatic perturbation theory, obtained with Eqs. (C3), (7), and (12).

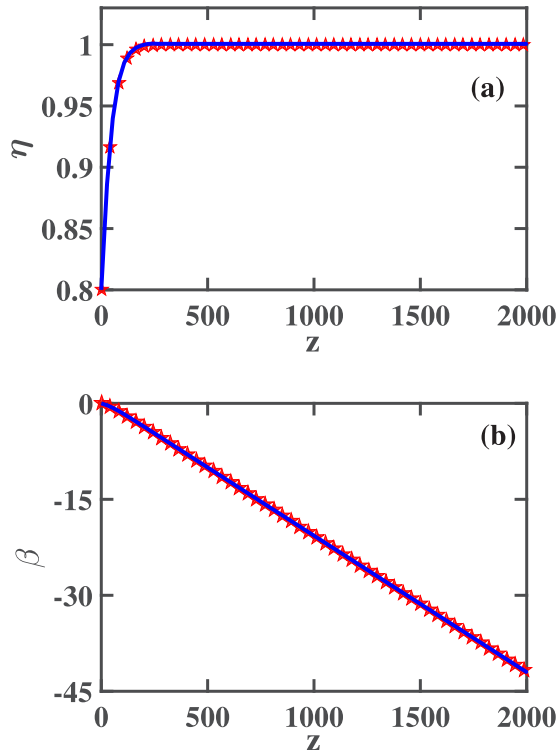


FIG. 12. The  $z$  dependence of the soliton amplitude  $\eta(z)$  (a) and frequency  $\beta(z)$  (b) for the closed optical waveguide loop setup considered in Figs. 9–11. The solid blue curves represent the results obtained by numerical simulations with Eqs. (14) and (15). The red stars correspond to the predictions of the adiabatic perturbation theory, obtained with Eq. (7) in (a) and with Eqs. (12) and (7) in (b).

predictions of the adiabatic perturbation theory, obtained with Eqs. (7) and (12). We observe that the numerically obtained soliton amplitude tends to the equilibrium value  $\eta_0 = 1$  at short distances and stays close to this value throughout the propagation, in excellent agreement with the perturbation theory prediction. Furthermore, the value of the soliton frequency obtained in the simulations remains close to the  $z$ -dependent value predicted by the adiabatic perturbation theory throughout the propagation. Thus, the efficient suppression of radiation emission in waveguides with frequency-dependent linear gain-loss, cubic loss, and delayed Raman response enables observation of stable amplitude and frequency dynamics along significantly larger distances compared with the distances obtained with the closed optical waveguide loop setup considered in Sec. III A. We also point out that the waveguide setups considered in the current subsection can be used for inducing large frequency shifts, which are not accompanied by pulse distortion, in soliton-based optical waveguide transmission systems.

#### IV. PULSE DYNAMICS IN WAVEGUIDES WITH LINEAR GAIN, CUBIC LOSS, AND GUIDING FILTERS

##### A. Introduction

The enhancement of transmission quality and stability in waveguides with frequency-dependent linear gain-loss and delayed Raman response, which was demonstrated in Sec. III B, is somewhat similar to transmission stability enhancement in waveguides with linear gain and guiding filters with a varying

central frequency. Indeed, in the latter waveguides, the guiding filters play a role similar to that of the frequency-dependent linear gain-loss, i.e., their presence leads to suppression of radiation emission with frequencies that are significantly different from the soliton's frequency. In addition, the variation of the central frequency of the guiding filters with propagation distance plays a role similar to that of the Raman self-frequency shift, that is, it leads to the separation of the soliton's Fourier spectrum from the radiation's Fourier spectrum. For this reason it is useful to compare the dynamics of optical solitons in the two waveguide systems. We therefore turn to study soliton propagation in optical waveguide loops with frequency-independent linear gain, cubic loss, and optical guiding filters. In this section, we briefly describe the results obtained for propagation in the presence of guiding filters with a constant central frequency. In Sec. IV B, we provide a detailed description of the results obtained for propagation in the presence of guiding filters with a varying central frequency. We point out that stabilization of soliton-based transmission in optical fibers by guiding filters with a varying central frequency was theoretically and experimentally demonstrated in Refs. [2,5,6,9,64]. Since these studies focused on optical fiber transmission, the effects of cubic loss were neglected. In this section, we extend the theoretical treatment of Refs. [2,5,64] and take into account the effects of cubic loss in addition to the effects of linear gain and guiding filters.

Let us briefly describe our results for soliton propagation in waveguide loops with frequency-independent linear gain, cubic loss, and guiding filters with a constant central frequency. According to the adiabatic perturbation theory, stable soliton propagation with constant amplitude  $\eta = \eta_0$  and frequency  $\beta = \omega_p$ , where  $\omega_p$  is the filtering frequency, is possible. However, stability analysis for small amplitude wave solutions of the linearized propagation model shows that these solutions are unstable at a frequency interval with a small width around the soliton's equilibrium frequency  $\omega_p$ . The same analysis also indicates that suppression of radiation emission by the guiding filters is more efficient at frequencies that are far from  $\omega_p$ . Numerical simulations with the full perturbed NLS model show that the soliton develops a radiative tail at short propagation distances and that the radiative tail is larger than the one observed in Sec. II for waveguides with linear gain or loss and cubic loss and with no guiding filters. As a result, transmission quality in waveguide loops with weak frequency-independent linear gain, cubic loss, and guiding filters with a constant central frequency is significantly reduced compared with the waveguide setups considered in Sec. II. The reduction in transmission quality is also manifested in the dynamics of the soliton's amplitude and frequency. Indeed, the numerically obtained curves of  $\eta(z)$  and  $\beta(z)$  deviate significantly from the curves predicted by the adiabatic perturbation theory at relatively short distances.

The reduction of transmission quality in waveguides with filters with a constant central frequency can be explained by analyzing the shape of the Fourier transform of the pulse. The emergence and growth of the radiative tail are manifested by a growing deviation of the numerically obtained shape of the Fourier transform of the pulse from the shape predicted by the adiabatic perturbation theory. This deviation appears as fast oscillations in the numerically obtained curve of the shape,

which are most pronounced at the instability interval around  $\omega_p$  of small amplitude wave solutions of the linearized propagation model. Moreover, there is no significant separation between the soliton's Fourier spectrum and the radiation's Fourier spectrum and, as a result, suppression of radiation by the filters is inefficient. The instability of small amplitude waves at frequencies near the equilibrium soliton's frequency  $\omega_p$  and the lack of separation between the soliton's and radiation's Fourier spectra are the key factors leading to the reduced transmission quality in waveguides with frequency-independent linear gain, cubic loss, and guiding filters with a constant central frequency.

### B. Waveguides with linear gain, cubic loss, and guiding filters with a varying central frequency

The drawbacks of the waveguide setup discussed in Sec. IV A can be circumvented by using guiding filters with a varying central frequency  $\omega_p(z)$ , which is a monotonous function of  $z$ . In this case at large distances, the soliton's spectrum is centered around a  $z$ -dependent frequency  $\tilde{\beta}_0 + \omega_p(z)$ , while the radiation's spectrum is centered near the constant frequency  $\tilde{\beta}_0$ . Since  $\omega_p(z)$  is a monotonous function of  $z$ , at sufficiently large  $z$   $|\omega_p(z)| \gg 1$ , and therefore the radiation's spectrum is well separated from the soliton's spectrum. As a result, in this case suppression of radiation emission by the guiding filters becomes very efficient at intermediate and large distances.

We therefore turn to study soliton propagation in the presence of weak linear gain, weak cubic loss, and guiding filters with a varying central frequency. Following the treatment in Refs. [2,5,64], we assume that the response function of the guiding filters can be approximated by a Gaussian with a maximum that is equal to 1 and that is located at the frequency  $\omega_p(z)$ . Under this assumption, the propagation is described by the following perturbed NLS equation [2,5,64]:

$$i\partial_z\psi + \partial_t^2\psi + 2|\psi|^2\psi = ig_0\psi/2 - i\epsilon_3|\psi|^2\psi - i\epsilon_\omega(i\partial_t - \omega_p)^2\psi, \quad (17)$$

where  $\epsilon_\omega$  is the second-order filtering coefficient, which satisfies  $0 < \epsilon_\omega \ll 1$ , and  $\omega_p$  is  $z$  dependent [65]. Equation (17) can also be written as

$$i\partial_z\psi + \partial_t^2\psi + 2|\psi|^2\psi = i(g_0/2 - \epsilon_\omega\omega_p^2)\psi - i\epsilon_3|\psi|^2\psi - 2\epsilon_\omega\omega_p\partial_t\psi + i\epsilon_\omega\partial_t^2\psi. \quad (18)$$

Using the adiabatic perturbation theory, we find that the dynamics of the soliton's amplitude and frequency is given by

$$\frac{d\eta}{dz} = \eta\{g_0 - 2\epsilon_\omega[\eta^2/3 + (\beta - \omega_p)^2] - 4\epsilon_3\eta^2/3\} \quad (19)$$

and

$$\frac{d\beta}{dz} = -4\epsilon_\omega(\beta - \omega_p)\eta^2/3. \quad (20)$$

Similar to the treatment in Refs. [2,5,64], we assume that  $\omega_p$  changes linearly with  $z$ , that is,  $\omega_p = \omega'_p z$ , where  $\omega'_p \equiv d\omega_p/dz = C_1$ , and  $C_1$  is a constant. We define a new frequency  $\tilde{\beta}$  by  $\tilde{\beta}(z) = \beta(z) - \omega_p(z)$ . The new system of equations for the dynamics of  $\eta$  and  $\tilde{\beta}$  is

$$\frac{d\eta}{dz} = \eta[g_0 - 2\epsilon_\omega(\eta^2/3 + \tilde{\beta}^2) - 4\epsilon_3\eta^2/3] \quad (21)$$

and

$$\frac{d\tilde{\beta}}{dz} = -C_1 - 4\epsilon_\omega\tilde{\beta}\eta^2/3. \quad (22)$$

We are interested in realizing stable transmission with constant amplitude  $\eta = \eta_0 > 0$  and frequency  $\tilde{\beta} = \tilde{\beta}_0 \neq 0$ . We therefore require that  $(\eta_0, \tilde{\beta}_0)$  is an equilibrium point of Eqs. (21) and (22). We obtain  $g_0 = 2\epsilon_\omega\eta_0^2/3 + 2\epsilon_\omega\tilde{\beta}_0^2 + 4\epsilon_3\eta_0^2/3$  and  $\tilde{\beta}_0 = -3\omega'_p/(4\epsilon_\omega\eta_0^2)$ . Thus, Eq. (21) takes the form

$$\frac{d\eta}{dz} = 2\eta[2\epsilon_3(\eta_0^2 - \eta^2)/3 + \epsilon_\omega(\eta_0^2 - \eta^2)/3 + \epsilon_\omega(\tilde{\beta}_0^2 - \tilde{\beta}^2)]. \quad (23)$$

Dynamics of the soliton's amplitude and frequency is therefore described by Eqs. (22) and (23). Linear stability analysis shows that  $(\eta_0, \tilde{\beta}_0)$  is a stable equilibrium point of the system (22) and (23) (a stable node), provided that  $\omega'_p$  satisfies the condition

$$|\omega'_p| < \left(\frac{8}{27}\right)^{1/2} \epsilon_\omega \left(1 + \frac{2\epsilon_3}{\epsilon_\omega}\right)^{1/2} \eta_0^3. \quad (24)$$

*Numerical simulations.* Equation (18) is numerically integrated on a domain  $[t_{\min}, t_{\max}] = [-400, 400]$  with periodic boundary conditions. The initial condition is in the form of an NLS soliton with amplitude  $\eta(0)$ , frequency  $\beta(0) = 0$ , position  $y(0) = 0$ , and phase  $\alpha(0) = 0$ . To enable comparison with the results of the numerical simulations for the waveguide setup considered in Sec. IV A, we use parameter values that are similar to the ones used in this section. In particular, we carry out the simulations with  $\epsilon_3 = 0.01$ ,  $\epsilon_\omega = 0.04$ ,  $\omega_p(0) = 0$ , and  $\eta(0) = 0.8$ . We realize efficient separation between the soliton's spectrum and the radiation's spectrum by choosing  $\omega'_p = 0.0218$ , which is close to the largest value allowed by inequality (24). We emphasize, however, that similar results are obtained for other values of the physical parameters. Similar to the simulations in Secs. III and IV A, the soliton passes multiple times through the computational domain's boundaries during the simulation and therefore the simulation describes soliton propagation in a closed waveguide loop. To avoid soliton destruction, we do not employ damping at the boundaries. The simulation is run up to a final propagation distance  $z_f = 2000$ , at which the value of the transmission quality integral  $I(z)$  is still smaller than 0.075.

Figure 13 shows the pulse shape  $|\psi(t, z)|$  at  $z = z_f$ , as obtained in the simulations. Also shown is the prediction of the adiabatic perturbation theory, obtained with Eqs. (C1), (22), and (23). As seen in Figs. 13(a) and 13(b), the numerically obtained pulse shape at  $z = z_f$  is very close to the analytic prediction and no significant radiative tail is observed. Furthermore, as seen in Fig. 13(c), the deviation of the numerical result for  $|\psi(t, z_f)|$  from the theoretical one is smaller than  $10^{-9}$  for all  $t$  values. Therefore, the introduction of guiding filters with a central frequency that changes linearly with propagation distance leads to significant enhancement of transmission quality compared with the waveguide setups considered in Secs. II, III A, and IV A. The enhancement of transmission quality is also demonstrated in Fig. 14, which shows the  $z$  dependence of the transmission quality integral  $I$  obtained in the simulations along with the average  $\langle I(z) \rangle$ . As seen in this figure, the value of  $I(z)$  is smaller than 0.05 throughout the

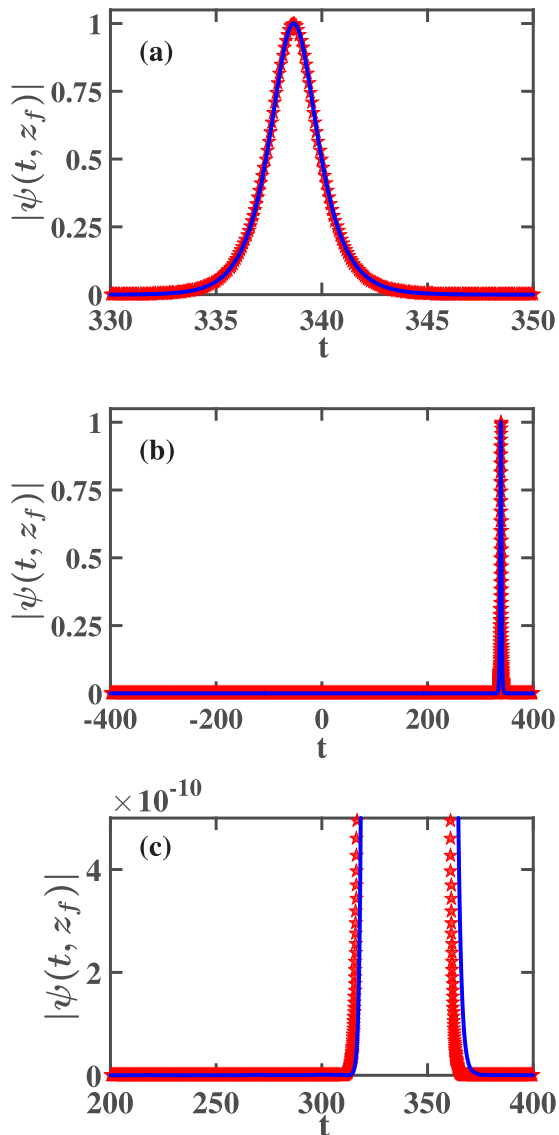


FIG. 13. The pulse shape  $|\psi(t, z_f)|$ , where  $z_f = 2000$ , for soliton propagation in a closed optical waveguide loop with weak frequency-independent linear gain, cubic loss, and guiding filters with a varying central frequency. The physical parameter values are  $\epsilon_3 = 0.01$ ,  $\epsilon_\omega = 0.04$ ,  $\omega_p(0) = 0$ ,  $\omega'_p = 0.0218$ ,  $\eta(0) = 0.8$ , and  $\beta(0) = 0$ . The solid blue curve represents the result obtained by numerical simulations with Eq. (18), while the red stars correspond to the prediction of the perturbation theory, obtained with Eqs. (C1), (22), and (23).

propagation and is smaller than 0.02 for  $96 \leq z \leq 2000$ . In addition,  $\langle I(z) \rangle = 0.00887$ .

Further insight into the enhanced transmission quality can be gained from the Fourier transform of the pulse  $|\hat{\psi}(\omega, z)|$ . Figure 15 shows the numerically obtained Fourier transform  $|\hat{\psi}(\omega, z)|$  at  $z = z_f$  together with the prediction of the adiabatic perturbation theory, obtained with Eqs. (C3), (22), and (23). The agreement between the two results is excellent. In particular, the Fourier transform  $|\hat{\psi}(\omega, z_f)|$  obtained in the simulation does not contain any fast oscillations in the main peak such as the oscillations seen in Fig. 3 in Sec. II B. Additionally,  $|\hat{\psi}(\omega, z_f)|$  does not contain any peaks associated with radiation emission such as the one seen in Fig. 7 in Sec. III A.

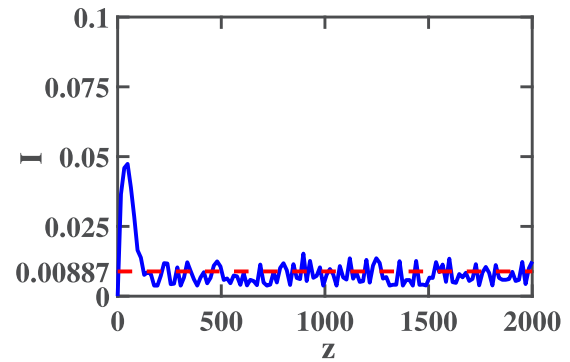


FIG. 14. The  $z$  dependence of the transmission quality integral  $I(z)$  obtained by numerical simulations with Eq. (18) for the same optical waveguide setup considered in Fig. 13. The solid blue curve represents  $I(z)$  and the dashed red horizontal line corresponds to  $\langle I(z) \rangle$ .

Based on these findings and based on the comparison with the results obtained in Sec. IV A, we deduce that the introduction of a varying central frequency of the guiding filters leads to significant enhancement of transmission quality. Similar to the situation in waveguides with delayed Raman response, the monotonous increase of the central filtering frequency  $\omega_p$  leads to separation of the soliton's spectrum from the radiation's

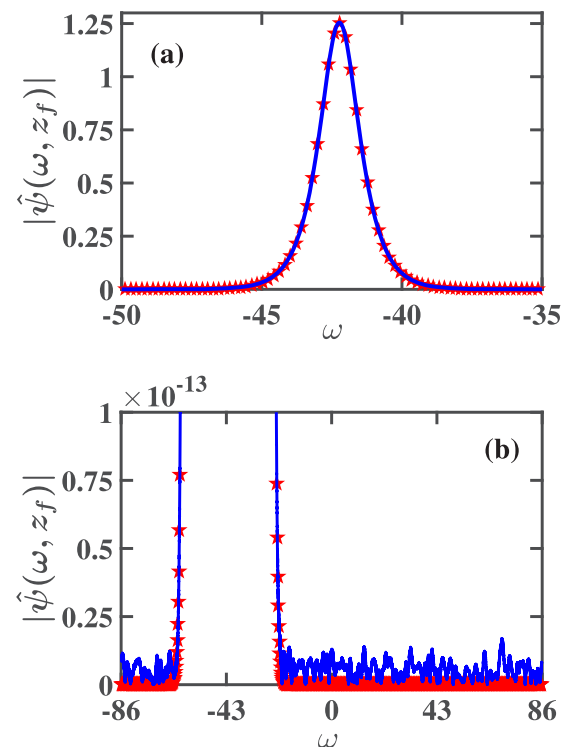


FIG. 15. The Fourier transform of the pulse shape  $|\hat{\psi}(\omega, z)|$  at  $z_f = 2000$  for soliton propagation in a closed optical waveguide loop with weak frequency-independent linear gain, cubic loss, and guiding filters with a varying central frequency. The physical parameter values are the same as in Fig. 13. The solid blue curve represents the result obtained by numerical simulations with Eq. (18). The red stars correspond to the prediction of the adiabatic perturbation theory, obtained with Eqs. (C3), (22), and (23).

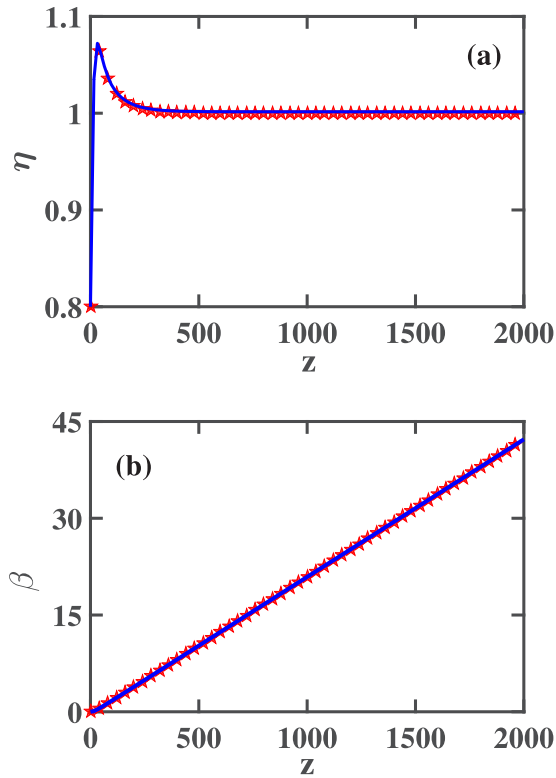


FIG. 16. The  $z$  dependence of the soliton amplitude  $\eta(z)$  (a) and frequency  $\beta(z)$  (b) for the closed optical waveguide loop setup considered in Figs. 13–15. The solid blue curves represent the results obtained by numerical simulations with Eq. (18). The red stars correspond to the predictions of the adiabatic perturbation theory, obtained with Eqs. (22) and (23).

spectrum. The separation of the two spectra enables efficient suppression of radiation emission with frequencies that are significantly different from the soliton’s frequency due to the presence of the guiding filters.

Figures 16(a) and 16(b) show the  $z$  dependence of the soliton’s amplitude and frequency obtained in numerical simulations with Eq. (18). Also shown are the predictions of the adiabatic perturbation theory, obtained with Eqs. (22) and (23). It is seen that the numerically obtained soliton amplitude tends to the equilibrium value  $\eta_0 = 1$  at short distances and stays close to this value throughout the propagation, in excellent agreement with the perturbation theory prediction. Additionally, the value of the soliton frequency obtained in the simulations remains close to the  $z$ -dependent value predicted by the adiabatic perturbation theory throughout the propagation. Based on these findings and on similar results obtained for other values of the physical parameters, we conclude that the efficient suppression of radiation emission in waveguides with frequency-independent linear gain, cubic loss, and guiding filters with a varying central frequency enables observation of stable amplitude and frequency dynamics along significantly larger distances compared with the distances obtained with the closed optical waveguide loop setups considered in Secs. III A and IV A. In this sense, stabilization of amplitude and frequency dynamics in waveguides with guiding filters with a varying central frequency is similar to the stabilization

observed in Fig. 12, for waveguides with frequency-dependent linear gain-loss, cubic loss, and delayed Raman response.

## V. CONCLUSIONS

We studied transmission stabilization against radiation emission for single-soliton propagation in nonlinear optical waveguides with weak linear gain-loss, cubic loss, and delayed Raman response. The value of the linear gain coefficient for waveguides with frequency-independent linear gain was chosen such that stable soliton transmission with a constant amplitude can be realized. However, the presence of the linear gain can lead to an unstable growth of small amplitude waves (radiation) emitted by the soliton. We therefore looked for ways for stabilizing the transmission by frequency-dependent linear gain-loss and delayed Raman response. We characterized transmission quality and stability by calculating the transmission quality integral, which measures the deviation of the pulse shape obtained in numerical simulations with perturbed NLS equations from the shape expected by the adiabatic perturbation theory for the NLS soliton. Additionally, we characterized stability of amplitude and frequency dynamics by comparing the numerically obtained  $z$  dependence of the soliton’s amplitude and frequency with the  $z$  dependence expected by the adiabatic perturbation theory.

We first studied soliton propagation in the absence of delayed Raman response. Our numerical simulations with the perturbed NLS propagation models showed that transmission quality in waveguides with frequency-independent linear gain and cubic loss is comparable to transmission quality in waveguides with frequency-dependent linear gain-loss and cubic loss. Furthermore, we found that in the absence of delayed Raman response, the presence of frequency-dependent linear gain-loss does not lead to enhancement of transmission quality due to the lack of significant separation between the soliton’s Fourier spectrum and the radiation’s Fourier spectrum.

We then included the effects of delayed Raman response in the perturbed NLS model. Our numerical simulations showed that in waveguides with frequency-independent linear gain, cubic loss, and delayed Raman response, the soliton’s spectrum becomes separated from the radiation’s spectrum due to the Raman self-frequency shift experienced by the soliton. However, in this case transmission quality was not improved compared with transmission quality in the absence of delayed Raman response due to the lack of an efficient mechanism for suppression of radiation emission. For the same reason, dynamics of the soliton’s amplitude and frequency became unstable at intermediate propagation distances.

Drastic enhancement of transmission quality and stability was demonstrated in waveguides with weak frequency-dependent linear gain-loss, cubic loss, and delayed Raman response. In this case, our numerical simulations showed that the presence of delayed Raman response leads to separation of the soliton’s spectrum from the radiation’s spectrum, while the presence of frequency-dependent linear gain-loss with relatively strong loss far from the soliton’s frequency leads to efficient suppression of radiation emission. This enabled the observation of distortion-free soliton propagation and stable amplitude and frequency dynamics along significantly larger distances compared with the distances obtained in the absence

of delayed Raman response and compared with the distances obtained in waveguides with frequency-independent linear gain, cubic loss, and delayed Raman response. Further numerical simulations showed that enhancement of transmission quality in waveguides with weak frequency-dependent linear gain-loss, cubic loss, and delayed Raman response is similar to transmission quality enhancement in waveguides with weak frequency-independent linear gain, cubic loss, and guiding filters with a varying central frequency. More specifically, the simulations demonstrated that the variation of the central filtering frequency leads to separation of the soliton's spectrum from the radiation's spectrum, while the presence of the guiding filters leads to efficient suppression of radiation emission. Thus, our study demonstrates a general mechanism for stabilizing transmission of optical solitons, which is based on the interplay between frequency-dependent linear gain-loss and perturbation-induced shifting of the soliton frequency.

### ACKNOWLEDGMENT

D.C. is grateful to the Mathematics Department of NJCU for providing technological support for the computations.

### APPENDIX A: ADIABATIC PERTURBATION THEORY FOR THE FUNDAMENTAL NLS SOLITON

In this appendix we give a brief summary of the adiabatic perturbation theory for the fundamental NLS soliton, which was developed by Kaup [53,57,66]. The theory was used for analyzing soliton dynamics in a variety of optical waveguide systems (see, e.g., Refs. [3,54] and references therein).

To illustrate the approach, consider the perturbed NLS equation

$$i\partial_z\psi + \partial_t^2\psi + 2|\psi|^2\psi = \epsilon h(t, z), \quad (\text{A1})$$

where  $0 < |\epsilon| \ll 1$ . We look for a solution of Eq. (A1) in the form

$$\begin{aligned} \psi(t, z) &= \psi_s(t, z) + \psi_{\text{rad}}(t, z) \\ &= \eta(z) \frac{\exp[i\chi(t, z)]}{\cosh(x)} + v(t, z) \exp[i\chi(t, z)], \end{aligned} \quad (\text{A2})$$

where  $x = \eta(z)[t - y(z)]$ ,  $\chi(t, z) = \alpha(z) - \beta(z)[t - y(z)]$ ,  $y(z) = y(0) - 2 \int_0^z dz' \beta(z')$ , and  $\alpha(z) = \alpha(0) + \int_0^z dz' [\eta^2(z') + \beta^2(z')]$ . The first term on the right-hand side of Eq. (A2) is the soliton solution with slow varying parameters, while the second term, which is of  $O(\epsilon)$ , is the radiation part. We now substitute Eq. (A2) into Eq. (A1) and keep terms up to  $O(\epsilon)$ . The resulting equation and its complex conjugate can be written in the following vector form:

$$\begin{aligned} & \frac{i}{\cosh(x)} \begin{pmatrix} 1 \\ -1 \end{pmatrix} \eta \left( \frac{d\alpha}{dz} + \beta \frac{dy}{dz} - \eta^2 + \beta^2 \right) \\ & + \frac{\tanh(x)}{\cosh(x)} \begin{pmatrix} 1 \\ 1 \end{pmatrix} \eta^2 \left( \frac{dy}{dz} + 2\beta \right) - \frac{ix}{\cosh(x)} \begin{pmatrix} 1 \\ -1 \end{pmatrix} \frac{d\beta}{dz} \\ & - \frac{[x \tanh(x) - 1]}{\cosh(x)} \begin{pmatrix} 1 \\ 1 \end{pmatrix} \frac{d\eta}{dz} + \partial_z \begin{pmatrix} v \\ v^* \end{pmatrix} - i\eta^2 \mathcal{L} \begin{pmatrix} v \\ v^* \end{pmatrix} \\ & - 2\beta \partial_t \begin{pmatrix} v \\ v^* \end{pmatrix} = -i\epsilon \begin{pmatrix} h(t, z)e^{-i\chi} \\ -h^*(t, z)e^{i\chi} \end{pmatrix}. \end{aligned} \quad (\text{A3})$$

The linear operator  $\mathcal{L}$  in Eq. (A3) is defined by

$$\mathcal{L} = (\partial_x^2 - 1)\sigma_3 + \frac{2}{\cosh^2(x)}(2\sigma_3 + i\sigma_2), \quad (\text{A4})$$

where  $\sigma_j$  with  $1 \leq j \leq 3$  are the Pauli spin matrices.

The complete set of orthogonal eigenfunctions of  $\mathcal{L}$  was found in Refs. [53,57,66]. It includes four localized eigenfunctions, which appear in the first four terms on the left-hand side of Eq. (A3):

$$\begin{aligned} f_0(x) &= \frac{1}{\cosh(x)} \begin{pmatrix} 1 \\ -1 \end{pmatrix}, & f_1(x) &= \frac{\tanh(x)}{\cosh(x)} \begin{pmatrix} 1 \\ 1 \end{pmatrix}, \\ f_2(x) &= \frac{x}{\cosh(x)} \begin{pmatrix} 1 \\ -1 \end{pmatrix}, & f_3(x) &= \frac{x \tanh(x) - 1}{\cosh(x)} \begin{pmatrix} 1 \\ 1 \end{pmatrix}. \end{aligned} \quad (\text{A5})$$

The eigenfunctions  $f_0(x)$  and  $f_1(x)$  have a zero eigenvalue, while  $f_2(x)$  and  $f_3(x)$  satisfy  $\mathcal{L}f_2 = -2f_1$  and  $\mathcal{L}f_3 = -2f_0$  [53,57,66]. The left localized eigenfunctions of  $\mathcal{L}$ , which are given by  $f_m^T \sigma_3$  for  $0 \leq m \leq 3$ , satisfy the following relations [53,57,66]:

$$\begin{aligned} \int_{-\infty}^{+\infty} dx f_2^T(x) \sigma_3 f_1(x) &= 2, \\ \int_{-\infty}^{+\infty} dx f_0^T(x) \sigma_3 f_3(x) &= -2. \end{aligned} \quad (\text{A6})$$

In addition, the set of eigenfunctions of  $\mathcal{L}$  contains an infinite set of unlocalized eigenfunctions, which are characterized by a continuous index  $q$ , where  $-\infty < q < \infty$ . We obtain the dynamic equations for the four soliton parameters by projecting both sides of Eq. (A3) on the four left localized eigenfunctions of  $\mathcal{L}$ . In particular, the equations for amplitude and frequency dynamics are obtained by projecting both sides of Eq. (A3) on the left eigenfunctions  $f_0^T(x) \sigma_3 = \text{sech}(x)(1, 1)$  and  $f_1^T(x) \sigma_3 = \text{sech}(x) \tanh(x)(1, -1)$ , respectively.

### APPENDIX B: AMPLITUDE DYNAMICS IN THE PRESENCE OF FREQUENCY-DEPENDENT LINEAR GAIN-LOSS

In this appendix we derive Eq. (5) for the dynamics of the soliton's amplitude in waveguides with frequency-dependent linear gain-loss and cubic loss. The calculation of the effects of cubic loss on amplitude dynamics is straightforward and has been presented in earlier works (see, e.g., Refs. [12,29]). We therefore concentrate mainly on calculating the effects of frequency-dependent linear gain-loss on amplitude dynamics.

We introduce the following notations for the two perturbation terms on the right-hand side of Eq. (1):  $h_1(t, z) = i\mathcal{F}^{-1}(\hat{g}(\omega)\hat{\psi})/2$  and  $h_2(t, z) = -i\epsilon_3|\psi|^2\psi$ , and assume that  $\hat{g}(\omega)$  can be approximated by Eq. (4). In the leading order of the perturbation theory, we approximate  $\psi$  and  $\hat{\psi}$  by the soliton parts  $\psi_s$  and  $\hat{\psi}_s$ , which are given by Eqs. (A2) and (C2), respectively. Therefore [67],

$$h_1(t, z) \simeq i\mathcal{F}^{-1}(\hat{g}(\omega)\hat{\psi}_s)/2 \quad (\text{B1})$$

and

$$h_2(t, z) \simeq -i\epsilon_3|\psi_s|^2\psi_s. \quad (\text{B2})$$



We first calculate the contribution of  $h_1(t, z)$  to the right-hand side of Eq. (5). Using the convolution theorem, we obtain

$$\mathcal{F}^{-1}(\hat{g}(\omega)\hat{\psi}_s) = (2\pi)^{-1/2} \int_{-\infty}^{\infty} ds g(s)\psi_s(t-s, z). \quad (\text{B3})$$

Calculation of the inverse Fourier transform of  $\hat{g}(\omega)$  yields

$$g(t) = -(2\pi)^{1/2} g_L \delta(t) + \left(\frac{2}{\pi}\right)^{1/2} (g_0 + g_L) \exp[-i\beta(0)t] \sin(Wt/2)/t, \quad (\text{B4})$$

where  $\delta(t)$  is the Dirac delta function. Substituting Eq. (B4) into Eq. (B3) while using the expression for  $\psi_s(t, z)$  in Eq. (A2), we obtain the following equation for the leading-order approximation for  $-ih_1(t, z)$ :

$$-ih_1(t, z) \simeq \frac{-g_L \eta e^{i\chi}}{2 \cosh(x)} + \frac{(g_0 + g_L)}{2\pi} \eta e^{i\chi} \int_{-\infty}^{\infty} ds \frac{\sin(Ws/2)}{s \cosh(x - \eta s)}. \quad (\text{B5})$$

From Eq. (B5) it follows that

$$-i \begin{pmatrix} h_1(t, z) e^{-i\chi} \\ -h_1^*(t, z) e^{i\chi} \end{pmatrix} \simeq \frac{-g_L \eta}{2 \cosh(x)} \begin{pmatrix} 1 \\ 1 \end{pmatrix} + \frac{(g_0 + g_L)}{2\pi} \eta \begin{pmatrix} 1 \\ 1 \end{pmatrix} \int_{-\infty}^{\infty} ds \frac{\sin(Ws/2)}{s \cosh(x - \eta s)}. \quad (\text{B6})$$

A straightforward calculation for the contribution of the cubic loss term yields

$$-i \begin{pmatrix} h_2(t, z) e^{-i\chi} \\ -h_2^*(t, z) e^{i\chi} \end{pmatrix} \simeq -\frac{\epsilon_3 \eta^3}{\cosh^3(x)} \begin{pmatrix} 1 \\ 1 \end{pmatrix}. \quad (\text{B7})$$

Substituting Eqs. (B6) and (B7) into Eq. (A3) and projecting both sides of the resulting equation on the left eigenfunction  $f_0^T(x)\sigma_3 = \text{sech}(x)(1, 1)$  of the linear operator  $\mathcal{L}$ , we obtain

$$\frac{d\eta}{dz} = [-g_L + (g_0 + g_L)\tilde{J}(\eta; W)/(2\pi) - 4\epsilon_3 \eta^2/3]\eta. \quad (\text{B8})$$

The function  $\tilde{J}(\eta; W)$  in Eq. (B8) is given by

$$\begin{aligned} \tilde{J}(\eta; W) &= \int_{-\infty}^{\infty} ds \frac{\sin(Ws/2)}{s} \int_{-\infty}^{\infty} \frac{dx}{\cosh(x) \cosh(x - \eta s)} \\ &= 2\pi \operatorname{sgn}(\eta) \tanh\left(\frac{\pi W}{4\eta}\right) \end{aligned} \quad (\text{B9})$$

for  $\eta \neq 0$ , where  $W > 0$  is used [67]. Substituting Eq. (B9) into Eq. (B8) and using the notation  $V = \pi W/(4\eta)$ , we obtain [68]

$$\frac{d\eta}{dz} = [-g_L + (g_0 + g_L) \operatorname{sgn}(\eta) \tanh(V) - 4\epsilon_3 \eta^2/3]\eta. \quad (\text{B10})$$

Since in the physical problem  $\eta \geq 0$ , we arrive at

$$\frac{d\eta}{dz} = [-g_L + (g_0 + g_L) \tanh(V) - 4\epsilon_3 \eta^2/3]\eta, \quad (\text{B11})$$

which is Eq. (5). The equation for frequency dynamics is obtained by substituting Eqs. (B6) and (B7) into Eq. (A3)

and projecting both sides of the resulting equation on the left eigenfunction  $f_1^T(x)\sigma_3 = \text{sech}(x) \tanh(x)(1, -1)$ . This calculation yields the equation  $d\beta/dz = 0$ .

We now discuss stability properties of the equilibrium points  $\eta = \eta_0$  and  $\eta = 0$  of Eq. (7). Stability of the equilibrium point  $\eta = 0$  is established in a more convenient manner with the help of Eq. (B10). We therefore use Eq. (B10) in the following analysis. Substituting Eq. (6) for  $g_0$  into Eq. (B10), we obtain

$$\begin{aligned} \frac{d\eta}{dz} &= \eta \left\{ g_L \left[ \frac{\operatorname{sgn}(\eta) \tanh(V)}{\tanh(V_0)} - 1 \right] \right. \\ &\quad \left. + \frac{4}{3} \epsilon_3 \left[ \eta_0^2 \frac{\operatorname{sgn}(\eta) \tanh(V)}{\tanh(V_0)} - \eta^2 \right] \right\}. \end{aligned} \quad (\text{B12})$$

Denote the right-hand side of Eq. (B12) by  $H(\eta)$ . It is straightforward to show that  $H(\eta) < 0$  for  $\eta > \eta_0$ ,  $H(\eta) > 0$  for  $0 < \eta < \eta_0$ , and  $H(\eta) < 0$  for  $-\eta_0 < \eta < 0$ . It follows that there are no additional equilibrium points with  $\eta > 0$ , and that  $\eta = \eta_0$  is a stable equilibrium point, while  $\eta = 0$  is an unstable equilibrium point. Thus, the number, locations, and stability properties of the equilibrium points of Eqs. (7) and (8) are the same.

### APPENDIX C: CALCULATION OF THE TRANSMISSION QUALITY INTEGRAL $I(z)$

In this appendix we present the method used for calculating the transmission quality integral  $I(z)$  and the transmission quality distance  $z_q$  from the results of the numerical simulations. In addition, we present the theoretical predictions for the soliton's shape and its Fourier transform, which were used in the analysis of transmission quality.

The theoretical prediction for the soliton's shape and the calculation of  $I(z)$  are based on the adiabatic perturbation theory for the NLS soliton (see Refs. [3,53,54,57] and Appendix A). According to the theory, the total optical field can be written as a sum of the soliton part  $\psi_s$  and the radiation part  $\psi_{\text{rad}}$ , where the soliton part is given by the expression for the soliton solution to the unperturbed NLS equation with slowly varying parameters [see Eq. (A2)]. We therefore take  $\psi_s(t, z)$  as the theoretical prediction for the soliton part, i.e.,  $\psi^{(\text{th})}(t, z) \equiv \psi_s(t, z) = \eta(z) \operatorname{sech}(x) \exp(i\chi)$ , where  $x$  and  $\chi$  were defined in Appendix A. Therefore, the theoretical prediction for the soliton's shape is given by

$$|\psi^{(\text{th})}(t, z)| = \eta(z) \operatorname{sech}\{\eta(z)[t - y(z)]\}, \quad (\text{C1})$$

where  $\eta(z)$  and  $y(z)$  can be calculated by solving the equations for  $d\eta/dz$  and  $dy/dz$ , which are obtained within the framework of the adiabatic perturbation theory. We point out that the value of  $y(z)$  is not changed by linear gain-loss and by cubic loss. In addition, the value of  $y(z)$  is affected by the Raman perturbation in first order in  $\epsilon_R$  only via the  $z$  dependence of the soliton's frequency. Therefore, in this paper, we calculate the value of  $\eta(z)$  in Eq. (C1) by solving the perturbation theory's equation for  $d\eta/dz$ , while the value of  $y(z)$  is measured from the results of the numerical simulations. The Fourier transform

of  $\psi_s(t, z)$  with respect to time is

$$\hat{\psi}_s(\omega, z) = \left(\frac{\pi}{2}\right)^{1/2} \frac{\exp[i\alpha(z) - i\omega y(z)]}{\cosh\{\pi[\omega + \beta(z)]/(2\eta(z))\}}. \quad (\text{C2})$$

Thus, the theoretical prediction for the Fourier transform of the soliton's shape is given by

$$|\hat{\psi}^{(\text{th})}(\omega, z)| = \left(\frac{\pi}{2}\right)^{1/2} \text{sech}\{\pi[\omega + \beta(z)]/(2\eta(z))\}, \quad (\text{C3})$$

where  $\eta(z)$  and  $\beta(z)$  are calculated by solving the equations for  $d\eta/dz$  and  $d\beta/dz$  that are obtained with the adiabatic perturbation theory.

The transmission quality integral  $I(z)$  measures the deviation of the pulse shape obtained in the numerical simulations  $|\psi^{(\text{num})}(t, z)|$  from the soliton's shape predicted by the adiabatic perturbation theory  $|\psi^{(\text{th})}(t, z)|$ . We use the same definition of  $I(z)$  that was used in Ref. [16] for characterizing transmission stability in multisequence soliton-based optical waveguide systems. Thus,  $I(z)$  is defined by the relation

$$I(z) = \tilde{I}^{(\text{dif})}(z)/\tilde{I}(z), \quad (\text{C4})$$

where  $\tilde{I}^{(\text{dif})}(z)$  and  $\tilde{I}(z)$  are defined by

$$\tilde{I}^{(\text{dif})}(z) = \left\{ \int_{t_{\min}}^{t_{\max}} dt [|\psi^{(\text{th})}(t, z)| - |\psi^{(\text{num})}(t, z)|]^2 \right\}^{1/2} \quad (\text{C5})$$

and

$$\tilde{I}(z) = \left[ \int_{t_{\min}}^{t_{\max}} dt |\psi^{(\text{th})}(t, z)|^2 \right]^{1/2}. \quad (\text{C6})$$

From this definition it is clear that  $I(z)$  measures both distortion in the pulse shape due to radiation emission and deviations of the numerically obtained values of the soliton's parameters from the values predicted by the adiabatic perturbation theory. The transmission quality distance  $z_q$  is defined as the distance at which the value of  $I(z)$  first exceeds a constant value  $C$ . In this paper we used  $C = 0.075$ . We emphasize, however, that the values of the transmission quality distance obtained by using this definition are not very sensitive to the value of the constant  $C$ . That is, we found that small changes in the value of  $C$  lead to small changes in the measured  $z_q$  values.

- 
- [1] G. P. Agrawal, *Nonlinear Fiber Optics* (Academic Press, San Diego, CA, 2001).
- [2] L. F. Mollenauer and J. P. Gordon, *Solitons in Optical Fibers: Fundamentals and Applications* (Academic Press, San Diego, CA, 2006).
- [3] A. Hasegawa and Y. Kodama, *Solitons in Optical Communications* (Clarendon Press, Oxford, 1995).
- [4] E. Iannone, F. Matera, A. Mecozzi, and M. Settembre, *Nonlinear Optical Communication Networks* (Wiley, New York, 1998).
- [5] L. F. Mollenauer, J. P. Gordon, and P. V. Mamyshev, in *Optical Fiber Telecommunications III*, edited by I. P. Kaminow and T. L. Koch (Academic Press, San Diego, CA, 1997), Chap. 12.
- [6] L. F. Mollenauer and P. V. Mamyshev, *IEEE J. Quantum Electron.* **34**, 2089 (1998).
- [7] M. Nakazawa, *IEEE J. Sel. Top. Quantum Electron.* **6**, 1332 (2000).
- [8] M. Nakazawa, E. Yamada, H. Kubota, and K. Suzuki, *Electron. Lett.* **27**, 1270 (1991).
- [9] L. F. Mollenauer, P. V. Mamyshev, and M. J. Neubelt, *Electron. Lett.* **32**, 471 (1996).
- [10] L. F. Mollenauer, A. Grant, X. Liu, X. Wei, C. Xie, and I. Kang, *Opt. Lett.* **28**, 2043 (2003).
- [11] Q. M. Nguyen and A. Peleg, *Opt. Commun.* **283**, 3500 (2010).
- [12] A. Peleg, Q. M. Nguyen, and Y. Chung, *Phys. Rev. A* **82**, 053830 (2010).
- [13] A. Peleg and Y. Chung, *Phys. Rev. A* **85**, 063828 (2012).
- [14] D. Chakraborty, A. Peleg, and J.-H. Jung, *Phys. Rev. A* **88**, 023845 (2013).
- [15] Q. M. Nguyen, A. Peleg, and T. P. Tran, *Phys. Rev. A* **91**, 013839 (2015).
- [16] A. Peleg, Q. M. Nguyen, and T. P. Tran, *Opt. Commun.* **380**, 41 (2016).
- [17] A. Peleg, Q. M. Nguyen, and T. T. Huynh, *Eur. Phys. J. D* **71**, 30 (2017).
- [18] A. Peleg and D. Chakraborty, *Commun. Nonlinear Sci. Numer. Simulat.* **63**, 145 (2018).
- [19] D. Chakraborty, A. Peleg, and Q. M. Nguyen, *Opt. Commun.* **371**, 252 (2016).
- [20] F. M. Mitschke and L. F. Mollenauer, *Opt. Lett.* **11**, 659 (1986).
- [21] J. P. Gordon, *Opt. Lett.* **11**, 662 (1986).
- [22] Y. Kodama and A. Hasegawa, *IEEE J. Quantum Electron.* **23**, 510 (1987).
- [23] R. W. Boyd, *Nonlinear Optics* (Academic Press, San Diego, CA, 2008).
- [24] Q. Lin, O. J. Painter, and G. P. Agrawal, *Opt. Express* **15**, 16604 (2007).
- [25] R. Dekker, N. Usechak, M. Först, and A. Driessen, *J. Phys. D: Appl. Phys.* **40**, R249 (2007).
- [26] G. S. He, L.-S. Tan, Q. Zheng, and P. N. Prasad, *Chem. Rev.* **108**, 1245 (2008).
- [27] Y. S. Kivshar and B. A. Malomed, *Rev. Mod. Phys.* **61**, 763 (1989).
- [28] V. Mizrahi, K. W. DeLong, G. I. Stegeman, M. A. Saifi, and M. J. Andrejco, *Opt. Lett.* **14**, 1140 (1989).
- [29] Y. Silberberg, *Opt. Lett.* **15**, 1005 (1990).
- [30] A. B. Aceves and J. V. Moloney, *Opt. Lett.* **17**, 1488 (1992).
- [31] G. S. He, J. D. Bhawalkar, C. F. Zhao, and P. N. Prasad, *Appl. Phys. Lett.* **67**, 2433 (1995).
- [32] V. V. Afanasjev, J. S. Aitchison, and Y. S. Kivshar, *Opt. Commun.* **116**, 331 (1995).
- [33] E. N. Tsoy, C. M. de Sterke, and F. Kh. Abdullaev, *J. Opt. Soc. Am. B* **18**, 1144 (2001).
- [34] O. Katz, Y. Lahini, and Y. Silberberg, *Opt. Lett.* **33**, 2830 (2008).
- [35] A. Peleg, Y. Chung, T. Dohnal, and Q. M. Nguyen, *Phys. Rev. E* **80**, 026602 (2009).
- [36] Y. Okawachi, O. Kuzucu, M. A. Foster, R. Salem, A. C. Turner-Foster, A. Biberman, N. Ophir, K. Bergman, M. Lipson, and A. L. Gaeta, *IEEE Photon. Technol. Lett.* **24**, 185 (2012).
- [37] M. A. Foster, A. C. Turner, M. Lipson, and A. L. Gaeta, *Opt. Express* **16**, 1300 (2008).

- [38] R. Soref, *IEEE J. Sel. Top. Quantum Electron.* **12**, 1678 (2006).
- [39] R. Jones, A. Liu, H. Rong, M. Paniccia, O. Cohen, and D. Hak, *Opt. Express* **13**, 1716 (2005).
- [40] S. F. Preble, Q. Xu, B. S. Schmidt, and M. Lipson, *Opt. Lett.* **30**, 2891 (2005).
- [41] Ö. Boyraz, P. Koonath, V. Raghunathan, and B. Jalali, *Opt. Express* **12**, 4094 (2004).
- [42] T. K. Liang, L. R. Nunes, T. Sakamoto, K. Sasagawa, T. Kawanishi, M. Tsuchiya, G. R. A. Priem, D. Van Thourhout, P. Dumon, R. Baets, and H. K. Tsang, *Opt. Express* **13**, 7298 (2005).
- [43] R. Salem, M. A. Foster, A. C. Turner, D. F. Geraghty, M. Lipson, and A. L. Gaeta, *Opt. Express* **15**, 7802 (2007).
- [44] E. Tien, N. S. Yuksek, F. Qian, and O. Boyraz, *Opt. Express* **15**, 6500 (2007).
- [45] T. K. Liang, L. R. Nunes, M. Tsuchiya, K. S. Abedin, T. Miyazaki, D. Van Thourhout, W. Bogaerts, P. Dumon, R. Baets, and H. K. Tsang, *Opt. Commun.* **265**, 171 (2006).
- [46] M. Xiong, L. Lei, Y. Ding, B. Huang, H. Ou, C. Peucheret, and X. Zhang, *Opt. Express* **21**, 25772 (2013).
- [47] L. Yin, Q. Lin, and G. P. Agrawal, *Opt. Lett.* **32**, 391 (2007).
- [48] *Raman Amplifiers for Telecommunications 1: Physical Principles*, edited by M. N. Islam (Springer, New York, 2004).
- [49] *Raman Amplification in Fiber Optical Communication Systems*, edited by C. Headley and G. P. Agrawal (Elsevier, San Diego, CA, 2005).
- [50] R. Claps, D. Dimitropoulos, V. Raghunathan, Y. Han, and B. Jalali, *Opt. Express* **11**, 1731 (2003).
- [51] Q. Xu, V. R. Almeida, and M. Lipson, *Opt. Express* **12**, 4437 (2004).
- [52] R. Jones, H. Rong, A. Liu, A. Fang, M. Paniccia, D. Hak, and O. Cohen, *Opt. Express* **13**, 519 (2005).
- [53] D. J. Kaup, *Phys. Rev. A* **44**, 4582 (1991).
- [54] M. Chertkov, Y. Chung, A. Dyachenko, I. Gabitov, I. Kolokolov, and V. Lebedev, *Phys. Rev. E* **67**, 036615 (2003).
- [55] The dimensionless distance  $z$  in Eq. (1) is  $z = X/(2L_D)$ , where  $X$  is the dimensional distance,  $L_D = \tau_0^2/|\tilde{\beta}_2|$  is the dispersion length,  $\tau_0$  is the soliton width, and  $\tilde{\beta}_2$  is the second-order dispersion coefficient. The dimensionless time is  $t = \tau/\tau_0$ , where  $\tau$  is time.  $\psi = (\gamma\tau_0^2/|\tilde{\beta}_2|)^{1/2}E$ , where  $E$  is the electric field and  $\gamma$  is the Kerr nonlinearity coefficient. The coefficients  $g_0$  and  $\epsilon_3$  are related to the dimensional linear gain and cubic loss coefficients  $\rho_1$  and  $\rho_3$  by  $g_0 = 2\tau_0^2\rho_1/|\tilde{\beta}_2|$  and  $\epsilon_3 = 2\rho_3/\gamma$ .
- [56] P. C. Becker, N. A. Olsson, and J. R. Simpson, *Erbium-Doped Fiber Amplifiers: Fundamentals and Technology* (Academic Press, San Diego, CA, 1999), Chap. 8.
- [57] D. J. Kaup, *Phys. Rev. A* **42**, 5689 (1990).
- [58] This setup corresponds to the one used in many soliton-based transmission experiments, where the pulses propagate with a prescribed peak power and the frequency difference between adjacent pulse sequences is much larger than the spectral width of the pulses [1,6,7].
- [59] J. Yang, *Nonlinear Waves in Integrable and Nonintegrable Systems* (SIAM, Philadelphia, 2010).
- [60] E. A. Kuznetsov, A. V. Mikhailov, and I. A. Shimokhin, *Physica D* **87**, 201 (1995).
- [61] J. Soneson and A. Peleg, *Physica D* **195**, 123 (2004).
- [62] The dimensionless Raman coefficient  $\epsilon_R$  in Eq. (11) is  $\epsilon_R = 2\tau_R/\tau_0$ , where  $\tau_R$  is a dimensional time constant, characterizing the nonlinear waveguide's delayed Raman response [1,63]. The time constant  $\tau_R$  can be determined from the slope of the Raman gain curve of the waveguide [1,63].
- [63] S. Chi and S. Wen, *Opt. Lett.* **14**, 1216 (1989).
- [64] L. F. Mollenauer, J. P. Gordon, and S. G. Evangelides, *Opt. Lett.* **17**, 1575 (1992).
- [65] The dimensionless second-order filtering coefficient  $\epsilon_\omega$  in Eq. (17) is  $\epsilon_\omega = 2\tilde{\epsilon}_\omega/|\tilde{\beta}_2|$ , where  $\tilde{\epsilon}_\omega$  is the dimensional second-order filtering coefficient. The dimensionless central filtering frequency is  $\omega_p = \tilde{\omega}_p\tau_0$ , where  $\tilde{\omega}_p$  is the dimensional central filtering frequency.
- [66] D. J. Kaup, *J. Math. Anal. Appl.* **54**, 849 (1976).
- [67] Note that for  $\eta(z) = 0$ ,  $\psi_s(t, z) \equiv 0$  and  $\hat{\psi}_s(\omega, z) \equiv 0$ . Therefore, in this case,  $h_1(t, z) = 0$  and  $d\eta/dz = 0$  in the leading order of the perturbation theory.
- [68] Note that the right-hand side of Eq. (B10) is a continuous function of  $\eta$  for any  $\eta$ , including  $\eta = 0$ . Additionally, the right-hand side of Eq. (B10) tends to 0 as  $\eta$  tends to 0, in accordance with the statements in Ref. [67].